ORCA – Online Research @ Cardiff

Citation for final published version:

Martin, Andrew J., Jamieson, John W., de Ronde, Cornel E. J., Humphris, Susan E., McDonald, Iain , Layne, Graham D., Piercey, Glenn and MacLeod, Christopher J. 2023. Trace metal and sulfur cycling in a hydrothermally active arc volcano: deep-sea drilling of the Brothers volcano, Kermadec arc, New Zealand. Mineralium Deposita 58 (2) , pp. 402-425. 10.1007/s00126-022-01135-x

Publishers page: http://dx.doi.org/10.1007/s00126-022-01135-x

Trace metal and sulfur cycling in a hydrothermally active arc volcano: Deep-sea drilling of the Brothers volcano, Kermadec arc, New Zealand.

Andrew J. Martin[1,2*], John W. Jamieson[1], Cornel E.J. de Ronde[3], Susan E. Humphris[4], Iain McDonald[5], Graham D. Layne[1], Glenn Piercey[6] and Christopher J. MacLeod[5]

[1] Department of Earth Sciences, Memorial University of Newfoundland, Canada

[2] Department of Geoscience, University of Nevada, Las Vegas, USA

[3] GNS Science, 1 Fairway Drive, Lower Hutt 5040, New Zealand

[4] Department of Geology & Geophysics, Woods Hole Oceanographic Institution, Woods Hole, Massachusetts 02543, USA

[5]School of Earth and Environmental Sciences, Cardiff University, UK

[6] MAF-IIC SIMS Facility, Memorial University of Newfoundland, Canada

*corresponding author: andrew.martin@unlv.edu

Key words: IODP, trace metal geochemistry, sulfur isotopes, pyrite, Brothers volcano

Statements and Declarations

All authors certify that they have no affiliations with or involvement in any organization or entity with any financial interest or non-financial interest in the subject matter or materials discussed in this manuscript.

Abstract

Brothers volcano, located on the Kermadec arc north of New Zealand, hosts two geochemically distinct hydrothermal systems. The NW Caldera and Upper Cone hydrothermal fields exhibit distinct fluid compositions that are significantly influenced by seawater and magmatic volatiles, respectively. In this study, we present trace metal chemistry and sulfur isotope compositions of pyrite within hydrothermally-altered volcanic rocks recovered from drill cores at depths of up to 429 m below the seafloor collected during the International Ocean Discovery Program's Expedition 376. Magmatic volatile-influenced alteration resulting in pyrophyllite ± natroalunite assemblages occurs at the Upper Cone and at the NW Caldera below 189 m. At the NW Caldera, a later seawater-derived hydrothermal fluid overprints magmatic volatile alteration forming chlorite-rich alteration. Pyrite at the Upper Cone is fine-grained, euhedral and enriched in Cu, As, Sb, Pb and Pt and has an average $\delta^{34}S$ composition of -5.5 ± 2.9‰ (1σ, $n = 32$). In contrast, pyrite associated with pyrophyllite-rich alteration at the older NW Caldera site is coarse-grained, subhedral and has higher Co, Se, Te and Bi contents but a comparable average $\delta^{34}S$ value of -4.8 ± 5.5‰ (1σ, $n = 26$). The difference in trace metal content between pyrite from pyrophyllite ± natroalunite assemblages at the NW Caldera and Upper Cone site indicates a change in the trace metal enrichment signature of pyrite with the age of the hydrothermal system. Pyrite from chlorite-rich alteration (NW Caldera) is depleted in Cu, Te and Bi relative to all magmatic volatile-influenced pyrite but has a similar average $\delta^{34}S$ composition of -4.6 ± 3.5‰ (1σ, $n = 20$). The similarity in trace metal enrichment signature and average $\delta^{34}S$ composition of pyrite, regardless of associated alteration mineral assemblage shows that the initial magmatic volatile trace metal signature and sulfur isotope composition of pyrite is preserved during fluid overprinting. The lower content of Cu, Te and Bi in pyrite from chlorite-rich alteration confirms the importance of seawater-derived hydrothermal fluids in metal mobilization and consequent formation of hydrothermal precipitates at the seafloor.

Introduction

The distribution of trace metals in sulfide minerals associated with seafloor hydrothermal systems is poorly constrained, with many studies focusing solely on samples collected from black smoker chimneys and massive sulfide deposits at the seafloor (Butler and Nesbitt 1999; Berkenbosch et al. 2012; Wohlgemuth-Ueberwasser et al. 2015). Only a few studies have collected samples from below the seafloor, including the active TAG mound (Humphris et al. 1995), Iheya North (Takai et al. 2011), PACMANUS (Binns et al. 2002) and Middle Valley (Fouqet et al. 1998).

Variations in the trace metal signature and content of sulfide minerals that precipitate during the mixing of magmatic vapour and fluid with seawater can constrain the physical (e.g., temperature) and chemical (e.g., pH) composition of the hydrothermal fluid from which they formed (e.g., Metz and Trefry 2000; Wohlgemuth-Ueberwasser et al. 2015; Fuchs et al. 2019). Pyrite is especially useful in constraining changes in fluid chemistry and metal sources, as it is ubiquitous in seafloor hydrothermal mineral deposits (Hannington et al. 2005). In addition, sulfur isotope analysis can be used to assess links between magmatic volatile influx and metal enrichment in seafloor hydrothermal systems (Herzig et al. 1998; de Ronde et al. 2011). When combined, trace metal chemistry and the sulfur isotopic composition of pyrite can determine subsurface fluid mixing regimes, variations in magmatic volatile degassing and can be used to assess the movement and sequestration of metals below the seafloor.

Direct influx of magmatic volatiles during the degassing of shallow magma reservoirs has been suggested as an important source of some metals in seafloor hydrothermal deposits (Yang and Scott 1996; Butterfield et al. 2011; de Ronde et al. 2011; 2019a; Keith et al. 2016; Berkenbosch et al. 2019; Patten et al. 2020). This is especially true in arc and back-arc hosted hydrothermal systems where magmas commonly reach volatile saturation (Wallace 2005; Edmonds and Wallace 2017). The addition of magmatic volatiles such as SO_2, H_2O, CO_2, HCl and HF are important for two reasons: i) they provide a source of acidity that can directly influence the solubility and transport of metals, and ii) magmatic degassing may provide a direct source of certain metals to the overlying hydrothermal systems (Yang and Scott 1996). Some authors have suggested that the enrichment of Te, Se, Au, Bi and Cu provides evidence for the addition of a magmatic volatile phase into seafloor hydrothermal systems (Berkenbosch et al. 2012; Keith et al. 2016; Martin et al. 2020), whereas others suggest enrichment in Pb, As, Sb, Hg, Mo, Ag and S (Petersen et al. 2002; Wohlgemuth-Ueberwasser et al. 2015; Berkenbosch et al. 2019; Patten et al. 2020). Hence, the trace metal enrichment signature associated with the addition of magmatic volatiles warrants further examination.

In addition to trace metal enrichment profiles, sulfur isotope ratios ($\delta^{34}S$) of sulfide minerals can be used to investigate contributions from different, isotopically distinct sources of sulfur in the hydrothermal fluids.

Sulfide minerals in arc and immature back-arc seafloor hydrothermal deposits commonly have $\delta^{34}S$ values that are <0‰, such as Hine Hina (Lau back-arc basin; Herzig et al. 1998), Conical Seamount (near Lihir Island: Petersen et al. 2002; Gemmell et al. 2004) or SuSu Knolls (Yeats et al. 2014) indicating that the disproportionation of SO_2 occurs widely in these environments forming ^{34}S depleted sulfides (Ohmoto and Lasaga 1982; Kusakabe et al. 2000; Peters et al. 2021).

Here we present the trace metal geochemistry and sulfur isotope composition ($\delta^{34}S$) of pyrite from below the seafloor at the Brothers volcano collected during the International Ocean Discovery Program's (IODP) Expedition 376: "Brothers Arc Flux". At Brothers, based on the alteration mineralogy of volcanic host rocks and the chemistry of vent fluid, both magmatic volatile and seawater-influenced hydrothermal systems have been identified (de Ronde et al. 2005, 2011, 2109a). The Upper Cone site represents a relatively young magmatic-hydrothermal system, whereas the NW Caldera site is older and contains evidence of both seawater-derived and magmatic volatile-influenced alteration (de Ronde et al. 2019a). These two distinct styles of hydrothermal venting (de Ronde et al. 2011) allow us to establish links between magmatic volatile influx and the enrichment of trace metals in pyrite, and how this signature is affected by later seawater-derived hydrothermal fluid overprinting. This makes the Brothers volcano an ideal location to evaluate how the trace metal and sulfur isotopic composition of pyrite varies between hydrothermal fields, with depth below the seafloor, and to link metal enrichment signatures to magmatic volatile influx, system age, and subsurface fluid mixing.

Brothers volcano

Brothers volcano is located in the southern part of the Kermadec-Tonga intraoceanic arc, north of New Zealand (de Ronde et al. 2012; Fig. 1). The volcano consists of an elongate NW-SE volcanic edifice with a prominent central caldera with a near continuous rim measuring 3 x 3.4 km (de Ronde et al. 2005; Embley et al. 2012; Fig. 2). The volcanic rocks within the volcano are largely dacitic with minor rhyolitic lavas and rare basaltic dikes (Wright and Gamble 1999; Haase et al. 2006; Timm et al. 2012; Wysoczanski et al. 2012).

In this study we present data collected during IODP Expedition 376 from two drill holes within Brothers volcano (Fig. 2A). Hole U1530A is located in the NW Caldera hydrothermal field on the faulted inner caldera wall at a water depth of 1594.9 meters below sea level (mbsl) where drilling penetrated to a depth of 453 mbsf with an overall core recovery rate of 16.9% (de Ronde et al. 2019b). Hole U1528D is located in a crater atop the volcanic Upper Cone at a water depth of 1229.1 mbsl where drilling penetrated to a maximum depth of 359 mbsf with an overall core recovery rate of 26.1% (de Ronde et al. 2019c).

Hydrothermal venting

Brothers volcano hosts five active and one inactive site of hydrothermal venting (de Ronde et al. 2005; Baker et al. 2012). In this study, we focus on the NW Caldera and Upper Cone fields that show morphologically and geochemically distinct styles of hydrothermal venting. Fluid flow at the NW Caldera vent field occurs on the inner caldera wall and is controlled by a series of ring faults (Fig. 2B; Embley et al. 2012; Caratori Tontini et al. 2012, 2019; de Ronde et al. 2019a). Here, high-temperature (up to 320 °C), moderately acidic (pH 3.2), gas poor fluids that contain high Cl contents (up to 787 mM/kg; Kleint et al. 2019) are actively venting and forming metal-sulfide-rich chimneys. In contrast, the Upper Cone is characterized by diffuse fluid venting forming native sulfur chimneys and Fe-oxide crusts (Fig. 2A; de Ronde et al. 2011; Kleint et al. 2019; Stucker et al. 2022). At the Upper Cone, vent fluids are highly acidic (pH 1.2) but with lower temperatures (maximum 122 °C) and contain elevated ΣSO_4 ($\leq$88.9 mM) and H_2S (5.0 mM) contents (de Ronde et al. 2011; Kleint et al. 2019).

Alteration mineralogy

The difference in fluid chemistry and temperature between the Upper Cone and NW Caldera vent sites is reflected in the alteration mineralogy of the underlying volcanic rocks (de Ronde et al. 2019a, b, c,).

Previous studies have identified five different alteration mineral assemblages, two at the NW Caldera and three at the Upper Cone (Fig. 3 and 4) (de Ronde et al. 2019b; Martin et al. 2022).

At the NW Caldera site, alteration containing chlorite + quartz + anhydrite + pyrite ± illite ± smectite, classified as chlorite + quartz alteration, formed from the circulation of high-temperature (~300 °C), moderately low-pH (3-4) seawater-derived hydrothermal fluids. In contrast, pyrophyllite + illite + anhydrite + quartz + pyrite ± rutile ± diaspore ± zunyite, classified as pyrophyllite + illite alteration, indicates the presence of high-temperature (>320 °C) acidic fluids (pH <3) (de Ronde et al. 2019c; Martin et al. 2022) (ESM 1, Table T1 for sample description). Based on the distribution of alteration minerals with depth below the seafloor, a two-stage model has been proposed for the magmatic-hydrothermal evolution of Brothers volcano (de Ronde et al. 2019a). At the NW Caldera, below 189 mbsf, magmatic volatile-influenced alteration containing pyrophyllite + illite is locally overprinted by a chlorite + quartz assemblage (Fig. 3A-1) (de Ronde et al. 2019a,b). Overprinting results from changes in near-surface permeability that occurred in response to caldera collapse, which facilitated seawater ingress along caldera bounding ring faults and through the fractured caldera floor (Caratori Tontini et al. 2019; de Ronde et al. 2019a). The circulation of modified seawater and its consequent interaction with the host rocks led to the remobilization of earlier formed (by the magmatic fluids) hypersaline metal-rich brines within the NW Caldera hydrothermal system, providing a metal source for overlying seafloor sulfide mineralization (de Ronde et al. 2011, 2019a; Berkenbosch et al. 2012; Gruen et al. 2014).

At the Upper Cone, samples that contain natroalunite + anhydrite + quartz + cristobalite ± illite ± native sulfur ± pyrite ± rutile, classified as natroalunite alteration, formed at high-temperatures (>300 °C) from low-pH (<1-2) "acid-sulfate" type fluids. Samples that contain pyrophyllite + natroalunite + anhydrite + quartz + cristobalite ± native sulfur ± pyrite ± rutile, classified here as natroalunite + pyrophyllite alteration, formed at comparably high-temperatures (~300 °C) but at lower water:rock ratios (Seewald et al. 2019). In contrast, some samples contain smectite + cristobalite + pyrite + anhydrite and primary igneous plagioclase is preserved, indicating regions of increased seawater influx characterized by lower fluid temperatures

(~180 °C) and a higher fluid pH (~5) (Martin et al. 2022). These three mineral assemblages occur intercalated at irregular depth intervals from the seafloor to the bottom of the hole at the Upper Cone (Fig. 4A-1).

Methods

Trace element geochemistry of pyrite

The trace metal content of pyrite was analyzed by laser ablation inductively coupled plasma mass spectrometry (LA-ICP-MS) using a New Wave Research UP213 UV laser coupled to an iCAP RQ ICP-MS ($n = 345$; ESM 1, Table T3-5). Point analyses were performed with a diameter of 40 µm in time resolved analysis mode at a frequency of 10 Hz. Acquisition lasted for 45 s and a gas blank was measured for 25 s prior to analysis. Analyte masses measured included: ^{59}Co, ^{60}Ni, ^{65}Cu, ^{66}Zn, ^{75}As, ^{77}Se, ^{99}Ru, ^{101}Ru, ^{103}Rh, ^{105}Pd, ^{106}Pd, ^{108}Pd, ^{109}Ag, ^{111}Cd, ^{121}Sb, ^{125}Te, ^{185}Re, ^{189}Os, ^{193}Ir, ^{195}Pt, ^{197}Au, ^{206}Pb and ^{209}Bi. Data correction and the subtraction of gas blanks was performed using Thermo Qtegra software. External calibration was performed on a series of in-house sulfide standards (see Prichard et al. 2013). The repeat analysis of standard UQAC FeS-1 during analysis yielded a relative standard deviation of <5% for all elements except Ni, Cu and Cd, which were 17, 17 and 26%, respectively (ESM 1, Table T2). Sulfur-33 was used as an internal standard for all LA-ICP-MS analyses. The sulfur content of pyrite was determined prior to LA-ICP-MS analysis using quantitative energy dispersive spectroscopy on a scanning electron microscope, yielding an average sulfur content of 54.1 ± 0.4 wt.% (1σ, $n = 359$; ESM 1, Table T6).

Sulfur isotope analysis

The sulfur isotope composition (δ^{34}S) of pyrite was determined using secondary ion mass spectrometry (SIMS) microanalysis. Seventy-eight analyses were performed across 28 polished mounts that represent the different alteration mineral assemblages identified at Brothers. Sample blocks were mounted in epoxy in aluminum retaining rings, polished, and coated with 300Å of Au prior to analysis to mitigate charging of the sample during ion bombardment. Samples were analyzed using a Cameca IMS 4f SIMS instrument at the Microanalysis Facility at Memorial University of Newfoundland following the analytical procedure detailed in Brueckner et al. (2015). Each sample was bombarded with a primary ion beam of 250-450 pA of Cs^+ accelerated through a potential of 10 keV and focused into a 10 μm diameter rastered spot. Negatively charged secondary ions were accelerated into the mass spectrometer using a potential of +4.5 keV. Prior to analysis, each spot was pre-sputtered for 120 s with a 10 μm rastered beam to exclude sulfur contamination from the sample surface. Reproducibility of results was calculated based on the repeat analysis of standard reference materials UL9 (pyrite - $\delta^{34}S$= 16.3‰) and KH87 (pyrite - $\delta^{34}S$= 0.4‰) and is typically better than ±0.4‰ (1σ, ESM 1, Table T7). All analyses are reported in standard notation (‰) relative to Vienna-Canyon Diablo Troilite (VCDT).

Results

Sample mineralogy

We retain the use of previous classifications based on alteration mineralogy with samples from the NW Caldera wall (Hole U1530A) classified into chlorite + quartz and pyrophyllite + illite alteration assemblages (de Ronde et al. 2019a,b; Martin et al. 2022). Pyrite in the chlorite + quartz alteration (Fig. 3A and B) is relatively coarse-grained (>0.2 mm) and subhedral to euhedral (Fig. 3D, E and F). In the pyrophyllite + illite-rich (Fig. 3C) samples, pyrite is associated with anhydrite veins that cut the wall rock alteration (Fig. 3G). Sphalerite occurs as micro-scale inclusions within subhedral coarse-grained (>0.2 mm) pyrite (Fig. 3H). Some pyrite grains in pyrophyllite-rich alteration are anhedral (Fig. 3I). When etched using NaOCl, pyrite grains exhibit a range of different internal zonation patterns (Fig. 3J to L). In pyrite from samples located near the seafloor (<31 mbsf), multiple radial zonations parallel to the grain margin that delineate overgrowths are present (Fig. 3J). In deeper samples from chlorite + quartz alteration, zonations in pyrite are more diffuse and appear chaotic with crystal faces poorly defined (Fig. 3K). Pyrite from pyrophyllite + illite alteration commonly contained radial zonations that are no longer parallel to the grain margin, delineating a relict inner core zone (Fig. 3L).

At the Upper Cone (Hole U1528D) natroalunite + pyrophyllite ± native sulfur alteration occurs preferentially along bleached selvage networks that overprint the brecciated matrix (Fig. 4A). In some samples where bleached selvages are absent and alteration is more pervasive, pyrophyllite is absent (Fig. 4B). In other samples, both pyrophyllite and natroalunite are absent and samples contain smectite with the preservation of primary plagioclase (Fig. 4C). In all samples, pyrite occurs as very finely disseminated euhedral to subhedral grains (Fig. 4D-I). Pyrite occurs intergrown in the sample matrix (Fig. 4 D-F), associated with natroalunite + anhydrite that replaces plagioclase (Fig. 4G), and infilling vugs (Fig 4. H and I) (de Ronde et al. 2019b). Pyrite from the Upper Cone rarely displayed any internal zonation (Fig. 4J). In aggregates of pyrite, some grains showed radial zonations parallel to the grain margins (Fig. 4K and L)

Pyrite chemistry

NW Caldera

Six representative polished mounts were analyzed from the chlorite + quartz alteration (*n= 53* spot analyses; Fig. 5, Table 1) and nine mounts from samples with pyrophyllite + illite alteration assemblages at the NW Caldera site (*n= 76* spot analyses; Fig. 5). The pattern of enrichment for all pyrites at both the Upper Cone and NW Caldera, regardless of alteration assemblage show a relative enrichment in Cu, Se, Te and Pb compared to other elements analyzed (e.g., As, Sb, Bi, Co; Fig. 5A). However, the trace metal content of pyrite is variable between the different alteration mineral assemblages (Fig. 5A). Pyrite from the chlorite + quartz-rich alteration is enriched in As, Sb, Au and Pb, and depleted in Co, Cu, Se, Te and Bi, relative to pyrite from pyrophyllite + illite alteration (Fig. 5). Pyrite from the pyrophyllite + illite samples of Hole U1530A is strongly enriched in Se and Co relative to pyrite from Hole 1528D of the Upper Cone (Fig 5A).

A moderate positive correlation is observed between Au and Ag (R^2=0.62), Pb (R^2=0.67), Te (R^2=0.69), and Bi (R^2=0.63) and a strong correlation between Re and Pt (R^2=0.89) in pyrite from chlorite + quartz samples. In pyrite from pyrophyllite + illite samples, a strong correlation exists between Zn and Cd (R^2= 0.92) with a moderate to strong correlation between Se and Cu (R^2=0.63) and Se and Ag (R^2=0.81) (ESM 1, Table T4).

In addition to the difference in trace metal content between alteration types, trends also exist with depth below the seafloor. Near seafloor chlorite-rich samples to a depth of 26 mbsf are strongly enriched in As, Sb, Pb and Ag relative to deeper samples (Fig. 6A). Cobalt, Zn, Se, Te and Bi contents of near seafloor samples were generally below detection limit (Fig. 6A). With increasing depth, the median Co content of pyrite increases, peaking at a depth of 314 mbsf with a median content of 90 ppm (*n= 7*), then decreases to similar contents observed for the shallow parts of the core. Pyrite in pyrophyllite + illite samples at a depth of between 232 and 415 mbsf contained median Cu, Sb and Pb contents below the detection limit (Fig. 6A).

Upper Cone

Pyrite was analyzed in 17 polished mounts from the Upper Cone site (*n= 216* spot analyses; Fig. 5, Table 1). Pyrite from the smectite + primary plagioclase samples is enriched in As, Te, Pb, and Bi relative to other alteration types for this site (Fig. 5D, F, H and M), and contains the highest total measured trace metal content at 429 ppm (*n= 28*). Natroalunite + pyrophyllite samples contain the highest median Cu and Se contents but have the lowest median Co, As and Bi contents (*n= 151*; Fig. 5). Pyrite from natroalunite-rich samples contain the highest median Sb content but have the lowest median Se and Te contents (*n= 37;* Fig. 5G and H).

In the smectite + primary plagioclase samples, a moderate to strong positive correlation occurs between As and Sb ($R^2 = 0.69$), Ag and Pb ($R^2 = 0.88$), Sb and Pb ($R^2 = 0.77$), and Au and Pb ($R^2 = 0.66$). In pyrite from the natroalunite + pyrophyllite samples, only Zn and Ag ($R^2 = 0.74$), and Cd ($R^2 = 0.55$) show notable correlation. In the natroalunite-rich samples, a strong positive correlation exists between Pt and Re ($R^2 = 0.95$) and Au ($R^2 = 0.87$), with a moderate correlation between Pb, Au and Ag ($R^2 = 0.64$) (ESM 1, Table T5).

In addition to variations in pyrite chemistry with alteration assemblage, the trace metal content of pyrite varies with depth below the seafloor at the Upper Cone site (Fig. 6B). Pyrite from the uppermost 153 mbsf of the core has a higher trace metal content relative to pyrite from samples deeper in the hole. For example, the median Cu content of pyrite above 153 mbsf is 493 ppm, decreasing to 107 ppm below this depth (Fig. 6B). Similar enrichments in Se, Bi and Te are also noted above 153 mbsf.

Sulfur isotopes

NW Caldera

The sulfur isotope composition of pyrite from NW Caldera Hole U1530A range from -13.2 to 3.8‰, with an average $\delta^{34}S$ value of -4.7 ± 4.4‰ (1σ, *n*= *46*). Pyrite from chlorite + quartz-rich samples range from -12.9‰ to 0.4‰ and have an average $\delta^{34}S$ value of -4.6 ± 3.5‰ (1σ, *n*= *26*), whereas pyrite from the pyrophyllite + illite samples range from -13.2‰ to 3.8‰ but with a similar average $\delta^{34}S$ value of -4.8 ± 5.5‰ (1σ, *n*= *20*; Fig. 7).

With the exception of pyrite from a pyrophyllite + illite sample, core section (65R1), located at a depth of 314 mbsf, the average $\delta^{34}S$ composition of all samples was <0‰ (Fig. 8A). Only minor trends are discernible between sulfur isotope composition and depth below seafloor (Fig. 8A). For example, in the uppermost 50 mbsf, average $\delta^{34}S$ values appear to broadly decrease with depth from -1.5‰ at 0.7 mbsf to -6.7‰ at a depth of ~40 mbsf (Fig. 8A). Below a depth of 189 mbsf, $\delta^{34}S$ values in pyrite become more sporadic and no trends are discernible.

Upper Cone

The sulfur isotopic composition of pyrite from the Upper Cone ranges between -12.2 and 0.3‰, with samples dominated by smectite + primary plagioclase having an average value of -6.4 ± 2.8‰ (1σ, *n*= *7*), compared with -5.2 ± 2.6‰ (1σ, *n*= *17*) and -5.0 ± 3.8‰ (1σ, *n*= *8*) for samples that contain only natroalunite and natroalunite + pyrophyllite, respectively. There is no systematic relationship between pyrite sulfur isotope composition and depth below the seafloor (Fig. 8B).

Discussion

Incorporation of trace metals in pyrite

Trace metal content in pyrite can occur in two ways: i) lattice bound substitution, or ii) nano- to micro-scale inclusions analyzed within the host pyrite (Huston et al. 1995; Reich et al. 2005; Deditius et al. 2011). The incorporation of metals via substitution is dependent on the ionic radii and difference in charge between the elements that are being substituted (Goldschmidt and Muir 1954). In pyrite, metals are incorporated either through the substitution of Fe^{2+} (e.g., Co^{2+}) or S^{2-} (e.g., Se^{2-}), with substitutions being either stoichiometric (e.g., Co) or non-stoichiometric (e.g., Au or As; Abraitis et al. 2004).

Pyrite is the only sulfide mineral observed at the Upper Cone site. At the NW Caldera site pyrite is the dominant sulfide mineral, with minor sphalerite (<5 modal %) occurring near the seafloor (<31 mbsf) and as micro-scale inclusions in pyrite at a depth of 314 mbsf (Fig. 3H; de Ronde et al. 2019c). The presence of a mono-mineralic sulfide system is important to note, as the co-precipitation of different sulfide minerals will affect the behaviour of the trace metals (Huston et al. 1995; Cook et al. 2009; George et al. 2016). For example, Cd is preferentially incorporated in sphalerite whereas Ag preferentially partitions into galena (George et al. 2016). Therefore, pyrite that is co-precipitated with sphalerite is expected to be depleted in Zn and Cd relative to other samples that contain only pyrite. As the majority of samples from Brothers volcano are essentially mono-mineralic, it is unlikely that variation in pyrite trace metal content is influenced by the co-precipitation of different sulfide minerals.

At Brothers, pyrite textures indicating disequilibrium precipitation such as colloform or dendritic grain morphologies (Large et al. 2009; Melekestseva et al. 2014; Wohlgemuth-Ueberwasser et al. 2015) are absent in sub-seafloor samples. There is no notable variation in pyrite texture with depth below the seafloor, nor is there any notable textural variation between NW Caldera and Upper Cone pyrites. Instead, all pyrite is disseminated and anhedral to euhedral, reflecting varying degrees of grain resorption and overgrowth that occurred during the dissolution and re-precipitation of pyrite as the mineral grain grew (Figs. 3 and 4).

Grain dissolution is most prevalent in Hole U1530A at the NW Caldera where pyrite in pyrophyllite + illite-rich samples is often anhedral and highly resorbed containing relict cores (Fig. 3I and L). Thus, differences in pyrite morphology at Brothers are not considered an important factor in controlling the distribution of trace metals.

Previous studies have characterized the solubility limits of different metals in pyrite, i.e., the maximum metal content that can be hosted as a lattice bound substitution; above this threshold inclusions can form (Huston et al. 1995). Elements such as Se, Te, Au, As and Co occur in low concentrations, less than the established solubility limit for pyrite (Huston et al. 1995) indicating that they are incorporated as a lattice bound substitution (Figs. 9 and 10). Incorporation in a lattice bound substitution is confirmed using time resolved analysis (TRA) where Bi, Co, Se, Ag, Sb and Bi have a flat and uniform TRA profile that mirrors major metals such as Fe (Fig. 9A and B). Mineral inclusions, detected as discrete spikes in the TRA profile, were present in some samples (Cook et al. 2009; Wohlgemuth-Ueberwasser et al. 2015). In a sample from Hole U1528D of the Upper Cone at 191 mbsf (Fig. 9B), the TRA profile for both Zn and Cu appears jagged with distinct peaks in Zn and Cu counts confirming the presence of mineral inclusions, most likely sphalerite and chalcopyrite (Fig. 9B). The occurrence of sphalerite inclusions is also indicated in pyrophyllite + illite samples at the NW Caldera by a strong positive correlation between Zn and Cd (R^2 = 0.92), which reflects preferential partitioning of Cd into sphalerite (Cook et al. 2009).

For Au in pyrite, all data plots below the solubility limit for Au hosted as Au^0 in nano- or mineral-scale inclusions (Fig. 10A), indicating that Au is incorporated as Au^{+1} in the pyrite crystal lattice (Reich et al. 2005; Deditius et al. 2014). This is further supported by the relatively flat ablation profile for Au indicating it is incorporated in a solid solution (Fig. 9A and B). Previous studies have shown that the incorporation of Te is influenced by As content due to distortions in the pyrite lattice that occur at elevated As contents (Fig. 10B; Reich et al. 2005; Keith et al. 2018a). A large proportion of Brothers pyrite data, especially from pyrite in the chlorite + quartz-rich samples, plot above the Te solubility line indicating that Te is hosted as both inclusions and to a lesser extent as a lattice bound substitution (Fig. 10B). A similar coupled relationship between As and Sb is also observed, indicating that As content is important in enhancing the substitution of Sb in pyrite at Brothers (Fig. 10C) (Arbraitis et al. 2004).

Trace element and sulfur isotopic variation in Brothers volcano

Influence of fluid parameters on trace metal composition of pyrite

The physical and chemical compositions of vent fluid (e.g., pH, temperature, salinity) at the NW Caldera and Upper Cone sites are distinctly different (de Ronde et al. 2011; Kleint et al. 2019; Stucker et al. 2022 indicating different sub-surface fluid mixing regimes and variable amounts of magmatic volatile influx between these sites. The formation of high-temperature (up to 320 °C; de Ronde et al. 2019a) black smokers and associated sulfide accumulations at the seafloor indicate that hydrothermal fluid at the NW Caldera did not cool substantially during its ascent through the hydrothermal system, indicating minimal sub-surface mixing between hydrothermal fluid and seawater recharge (Caratori Tontini et al. 2019). At the Upper Cone, the temperature of venting fluid at the seafloor is notably less (maximum 122 °C) than the maximum homogenization temperature of 357 °C measured in fluid inclusions in core sampled below the seafloor (de Ronde et al. 2019c). This difference in temperature indicates that extensive subsurface mixing between magmatic-hydrothermal fluids and seawater has taken place, where seawater is entrained through the walls of the Upper Cone, prior to the venting of the fluid at the seafloor (de Ronde et al. 2011; Caratori Tontini et al. 2019; Kleint et al. 2019; Stucker et al. 2022).

Understanding variations in subsurface fluid flow is important, as the temperature and pH of the hydrothermal fluid influences the solubility, incorporation and content of trace metals in pyrite (Metz and Trefry, 2000; Wohlgemuth-Ueberwasser et al. 2015). Pyrite precipitated from low-temperature fluid (<250 °C) is observed to be enriched in Au, As, Zn, Cd, Ag and Sb as these metals are stable in lower temperature hydrothermal fluids (Hannington et al. 1995; Monecke et al. 2016). In contrast, at high-temperatures (>300 °C) pyrite is enriched in Co, Te, Se, Bi and Cu (Large 1992; Butler and Nesbitt 1999; Grant et al. 2018). The approximate formation temperature of samples from below the seafloor at Brothers has been constrained using alteration mineralogy, fluid inclusion analysis on drill core samples and the direct measurement of borehole fluid temperature (de Ronde et al. 2011, 2019b, c). The lowest temperature mineral assemblage of smectite with preservation of primary plagioclase at the Upper Cone formed at temperatures of ~180 °C (Reyes 1990) and pyrite in these samples is enriched in As, Te, Pb, and Bi (Fig. 5A and 10C). However, the enrichment of pyrite in Te and Bi is not consistent with pyrite formation at low-temperatures, indicating an additional control on the distribution of trace metals.

At the NW Caldera, pyrophyllite + illite alteration that formed at temperatures in excess of 300 °C contains the highest median Co and Se content in pyrite, although the pyrite is depleted in As, Sb and Pb. High Co and Se contents are consistent with the formation of pyrite at high-temperatures (Fig. 5A). However, pyrite from the chlorite + quartz alteration that also formed at high-temperatures (>280 °C) is relatively depleted in Se, Te, Co and Bi compared to pyrite in pyrophyllite + illite alteration, again indicating an additional control on the distribution of metals in pyrite at Brothers.

Phase separation is inferred to be an important process at the NW Caldera and Upper Cone sites (de Ronde et al. 2019a; Kleint et al. 2019; Diehl et al. 2020). At the NW Caldera, vent fluids exhibit both low and high chlorinity (310 to 751 mM; Kleint et al. 2019) relative to seawater, indicating that phase separation of the hydrothermal fluid is occurring. At the NW Caldera, anhydrite and quartz hosted fluid inclusions contain salinities of ~10 wt.% NaCl, suggesting boiling or flashing of the fluid during depressurisation, and inclusions with a salinity of ~45 wt.% NaCl equivalent that formed during the exsolution of a brine from a silicate melt (de Ronde et al. 2019a). At the Upper Cone, fluid inclusion salinities range from less than seawater (<3.2 wt.% NaCl equivalent) to ~40 wt.% NaCl equivalent (de Ronde et al. 2091a, c). The highly variable NaCl content of fluid inclusions at the Upper Cone provides evidence of vapour condensation during cooling, flashing or boiling of ascending fluid and, in the case of highly saline brines, direct exsolution from a silicate melt (de Ronde et al. 2019a,c).

Phase separation affects the concentration and distribution of trace metals in pyrite (Román et al. 2019). The partitioning of trace metals reflects the preferential segregation of Se, Te, Hg, Bi, Tl and volatiles (H_2S, CO_2, SO_2) into the vapor phase whilst Fe, Ni, Co, Pb and Zn are concentrated in the liquid phase and As and Sb do not show any preferential partitioning during segregation (Pokrovski et al. 2013). Hence, the ratio of Bi/Pb or Sb/Pb can be used to distinguish between boiling and non-boiling assemblages (Fig. 10D) (Román et al. 2019; Nestmeyer et al. 2021).

At the NW Caldera, samples from chlorite + quartz alteration located at ~31 mbsf and a single analysis from pyrophyllite + illite alteration plot within the boiling induced precipitation field of Román et al. (2019) (Bi/Pb (<0.03) and Sb/Pb (<0.5)), providing evidence that phase separation is occurring in the shallow part of the NW Caldera hydrothermal system (Fig. 10D). At the Upper Cone, pyrite plots within the boiling field, providing evidence that phase separation is occurring throughout the Upper Cone (Fig. 10D). However, interpreting these trace metal enrichment signatures is complicated by the addition of metals from magmatic volatile degassing (Bi; Berkenbosch et al. 2019) or the remobilization of metals after initial pyrite formation.

Magmatic volatile degassing

The degassing of volatiles (e.g., SO_2, CO_2, HCl, H_2O) from shallow, volatile-saturated magma chambers in arc and back-arc hosted hydrothermal systems, has been suggested as a source of some metals in overlying seafloor hydrothermal deposits (Hedenquist and Lowenstern 1994; Yang and Scott 2002, 1996; de Ronde et al. 2011; Edmonds and Wallace 2017). The specific metal enrichment signature associated with this process remains actively debated, with previous studies indicating an enrichment in Cu, Se, Te, Au, Bi, As, Hg, Sb and Tl as evidence for magmatic volatile influx (Large 1992; de Ronde et al. 2011; Berkenbosch et al. 2012, 2019; Wohlgemuth-Ueberwasser et al. 2015; Keith et al. 2016; Martin et al. 2020; Patten et al. 2020).

To investigate the effect of magmatic volatile influx on trace metal signatures in pyrite, we compare pyrite from natroalunite and pyrophyllite-bearing alteration at both the Upper Cone and NW Caldera sites, with pyrite from chlorite + quartz alteration zones that represent magmatic and seawater-overprinted end member alteration types, respectively. We find that Co, Cu, Se, Te and Bi contents are highest in pyrite from pyrophyllite-rich alteration compared with pyrite that has been overprinted by seawater (Fig. 5 and

10). A similar signature has previously been identified in pyrite from arc related seafloor hydrothermal deposits (e.g., Hine Hina, or Volcano 19; Fig. 10), showing that increased Co, Cu, Se, Te and Bi contents in pyrite are a consequence of magmatic volatile degassing. This trace metal signature is in good agreement with previous studies that attribute the enrichment of Au, Te, Bi, Cu, Mo, Ag and Se in black smoker chimneys at the Brothers NW Caldera site to magmatic volatile degassing (Berkenbosch et al. 2019).

Elevated Se contents are widely used as an indicator of magmatic volatile influx in seafloor hydrothermal deposits and ancient volcanogenic massive sulfide deposits (Layton-Matthews et al. 2013). Experimental modelling indicates that Se incorporation in pyrite is enhanced at low-temperatures (<150 °C) under oxidizing fluid conditions (Huston et al. 1995). Therefore, Se in pyrite from natroalunite bearing alteration at the Upper Cone should contain elevated Se contents relative to all other samples, as alteration fluids are oxidizing and magmatic volatiles are actively degassing; however, this is not the case. We attribute the relative depletion of Se in pyrite from samples containing natroalunite at the Upper Cone to mineral scale partitioning of Se between coexisting native sulfur and pyrite. Natroalunite bearing alteration contains native sulfur that commonly occurs infilling secondary porosity (Fig. 4A) indicating that it formed through SO_2 disproportionation during mixing with seawater (de Ronde et al. 2011). Native sulfur analyzed from the Kueishantao volcano (offshore Taiwan), Daikoku and Nikko volcanoes (Mariana arc) and Macauley cone (Kermadec arc) contained a median Se content of 1305 ppm ($n= 56$; Zeng et al. 2007; de Ronde et al. 2015). This demonstrates the ability of native sulfur to incorporate high concentrations of Se; however, this has not been confirmed at Brothers as no native sulfur was analyzed in this study.

Sulfur isotope ratios in pyrite provide further evidence supporting the influx of magmatic volatiles at Brothers. In MOR-hosted hydrothermal deposits, sulfur is leached from oceanic lithosphere, contained primary magmatic sulfide minerals (~0.1 ± 0.5‰; Sakai et al. 1984) and the thermochemical sulfate reduction (TSR) of seawater (~21 ± 0.2‰; Rees et al. 1978). In unsedimented arc and back-arc environments, isotopically light sulfur is produced during disproportionation of SO_2 from the degassing of underlying magma chambers, producing sulfide minerals with a $\delta^{34}S$ composition <0‰ (Herzig et al. 1998;

de Ronde et al. 2011). Upon mixing with hydrothermal fluid and cooling below ~400 °C, SO_2 undergoes disproportionation, producing both oxidized SO_4^{2-} and reduced H_2S (Giggenbach 1996; Kusakabe et al. 2000). During disproportionation, SO_4^{2-} becomes enriched whilst H_2S becomes depleted in ^{34}S relative to the starting SO_2 isotopic composition. The amount of fractionation between sulfur species is dependent on temperature and the relative amount of reduced and oxidized sulfur species produced (Kusakabe et al. 2000; McDermott et al. 2015).

Previous sulfur isotope studies of sulfide chimneys and mineralized crusts from the seafloor at Brothers describe largely negative $\delta^{34}S$ values for pyrite, ranging from -5.6 to 2.1‰, with an average of -2.3 ± 1.9‰ (1σ, *n= 25*, Fig. 11; de Ronde et al. 2003, 2011, 2005). When compiled based on location, pyrite separates recovered from the Upper Cone have an average $\delta^{34}S$ value of -4.5 ± 0.7‰ (1σ, *n=4*; de Ronde et al. 2005) whilst native sulfur has a lower average $\delta^{34}S$ value of -5.3 ± 1.9‰ (1σ; *n=14*) and vent fluid HS^- averages -3.6 ± 2.1‰ (1σ, *n= 4*) (de Ronde et al. 2005, 2011). Pyrite from the NW Caldera averages -1.2 ± 2.2‰ (1σ, *n= 24*), sphalerite -2.1 ± 1.8‰ (1σ, *n= 27*), chalcopyrite -2.6 ± 1.5‰ (1σ, *n= 9*) and vent fluid HS^- -1.1 ± 0.7‰ (1σ, *n= 6*; de Ronde et al. 2003, 2005, 2011) (Fig. 11).

The predominantly negative sulfur isotope values in pyrite, native sulfur and vent fluid HS^- at the Upper Cone site has previously been attributed to the disproportionation of SO_2 degassed from an underlying magma chamber. In contrast, the occurrence of both low and high $\delta^{34}S$ values in sulfide minerals and vent fluid HS^- from the NW Caldera indicate that sulfur is sourced from a combination of SO_2 disproportionation, the leaching of host rocks and TSR of seawater (de Ronde et al. 2003, 2005, 2011).

The sulfur isotopic composition of pyrite in this study is broadly consistent with previous interpretations at Brothers that indicate widespread disproportion of SO_2 (Fig. 6). However, our data for pyrite shows a greater range than that of the previous studies, with values ranging from -13.2 to 3.8‰ at the NW Caldera, and -12.2 to 0.3‰ at the Upper Cone (Fig. 6). High values up to 3.8‰ could indicate TSR of seawater or the reduction of SO_4^{2-} produced during the disproportionation of SO_2. However, multiple sulfur isotope analysis of pyrite ($\Delta^{33}S$) is needed to investigate this further (McDermott et al. 2015).

Influence of seawater overprinting at the NW Caldera site

In Hole U1530A of the NW Caldera site, alteration associated with magmatic volatiles is overprinted by a chlorite + quartz-rich alteration assemblage in intervals below 189 mbsf, indicative of the interaction of seawater-derived hydrothermal fluids with the volcanic host rocks at temperatures >300 °C (Humphris and Thompson 1978). Mass balance calculations in oceanic crust have shown that metals are leached from host rocks during fluid-rock interactions under similar conditions (Richardson et al. 1987; Banerjee et al. 2000). This is important, as the leaching of metals from host rocks and their contained sulfide minerals can provide a source of metals for the overlying seafloor hydrothermal deposits.

Pyrites from the seawater-influenced chlorite-rich overprinting alteration zones have a different trace metal content compared to pyrites in the pyrophyllite ± natroalunite alteration zones (Fig. 5 and 10). That is, Cu, Bi and Te are relatively depleted in pyrite from seawater alteration assemblages when compared to pyrite from the magmatic volatile assemblages. This provides evidence for the leaching and remobilization of Cu, Bi and Te during the overprinting of magmatic volatile alteration by seawater-derived hydrothermal fluid. Moreover, the total measured trace metal content of pyrite from seawater-influenced samples is the lowest measured in our dataset at 173 ppm, indicating that metals have been removed. The remobilization of metals from pyrite provides a potential source of metals for black smoker chimneys at the seafloor that are enriched in Cu (up to 28 wt.%) and contain Te and Bi-rich minerals such as tellurobismuthite (de Ronde et al. 2011; Berkenbosch et al. 2012). A depletion in Cu, Te and Bi in pyrite from overprinting chlorite + quartz alteration corroborates previous interpretations that suggest the remobilization of metals at the NW Caldera by late-stage seawater-derived hydrothermal fluids (de Ronde et al. 2019a). Moreover, if pyrite from chlorite + quartz alteration was solely precipitated during later seawater overprinting then it is expected to have higher $\delta^{34}S$ values (>0‰) due to the contribution of sulfur from TSR of seawater, and this is not the case.

Textural analysis of pyrite confirms that it did not undergo complete dissolution during fluid overprinting, instead undergoing metal leaching and recrystallization (Fig. 3K). Pyrite from the Upper Cone contains sharp zonations that occur parallel to the grain margin (Fig. 4K and L), similar to those present in pyrite from near seafloor samples (30 mbsf) at the NW Caldera (Fig. 3J). In deeper chlorite-rich samples that have been overprinted, pyrite exhibits diffuse poorly defined zonations, relict crystal faces, inclusions of anhydrite, and regions of complex growth zonation that are often chaotic in nature (Fig. 3K). We suggest that these features form when aggregates of fine-grained pyrite such as those observed at the Upper Cone (Fig. 4H) undergo recrystallization leading to the preservation of relict grain boundaries as zonations within a now larger mineral grain (Fig. 3K). In addition to geochemical and isotopic evidence, the preservation of zonations with diffuse margins and complex recrystallization textures support the observation that pyrite did not undergo complete dissolution during seawater overprinting.

The distribution of trace metals with depth below the seafloor

At the NW Caldera site, Hole U1530A, the distribution of trace metals in pyrite from chlorite-rich alteration shows a pronounced change with depth below the seafloor. At the seafloor and to a depth of ~30 mbsf, As, Sb, Ag and Pb are strongly enriched in pyrite whilst metals that are associated with higher-temperature fluids (>300 °C) are strongly depleted, including Co, Te, Se and Bi - with all or most analyses below the detection limit for these elements (Fig. 6A). The suite of metals enriched in the uppermost 30 mbsf of Hole U1530A, in chlorite-rich alteration, is best explained by a high-degree of seawater influx that lowers fluid temperature leading to an enrichment in metals such as As, Ag and Pb that are stable in lower temperature fluids (<300 °C) (Tivey et al. 1995; Edmonds et al. 1996). Heat flow modelling and near-seafloor magnetic data indicate that ascending high-temperature (>300 °C) hydrothermal fluid did not undergo large amounts of cooling during mixing with seawater at the NW Caldera (Caratori Tontini et al. 2012; 2019). Hence As, Ag, Sb and Pb will remain in solution, precipitating near the seafloor (~30 mbsf) where seawater mixing during shallow recharge is high and the fluid temperature is lower.

Above 153 mbsf all the way to the seafloor at the Upper Cone site, Cu, Zn, Se, Sb, Ag, Te, Pb and Bi are enriched in pyrite relative to samples below this depth, which are slightly enriched in Co and As (Fig. 6B). It is unlikely that this difference relates to a sampling bias as samples from both above and below 153 mbsf contain pyrite from all three alteration assemblages. Heat flow modelling and near seafloor magnetic data indicate that seawater recharge occurs through the flanks of the Upper Cone (Caratori-Tontini et al. 2012, 2019), lowering the temperature of the ascending hydrothermal fluid and enhancing metal precipitation efficiency, thus explaining the higher metal content of pyrite close to the seafloor (Edmonds et al. 1996; Metz and Trefry 2000).

Trace metal and sulfur cycling in a hydrothermally active arc volcano

The trace metal enrichment signature of sub-seafloor pyrite at Brothers is relatively homogenous between the different sites and alteration assemblages. However, trace metal contents exhibit some variation between pyrite associated with magmatic volatile influenced pyrophyllite + natroalunite alteration at the Upper Cone and NW Caldera (<189 mbsf) and those that have been overprinted by seawater-derived hydrothermal fluids represented by chlorite-rich alteration.

Pyrite analyzed from drill core from the Upper Cone (Hole U1528D) and pyrophyllite + illite alteration from the NW Caldera (Hole U1530A) exhibit the same metal enrichment signature; however the trace metal content of pyrite between the two sites differs slightly (Fig. 5A and B). Our data indicate that pyrite initially has a higher Cu, As, Sb, Pb and Pt content at the younger Upper Cone site with pyrite becoming progressively enriched in Co, Se, Te and Bi over time, which is observed in pyrite at the older NW Caldera site (Ditchburn and de Ronde 2017). The enrichment of Co, Se, Te and Bi relates to the prolonged exposure and recrystallization of older pyrite generations at the NW Caldera site (<189 mbsf; Ditchburn and de Ronde 2017) due to the influx of magmatic volatiles. We interpret the enrichment of Co to indicate higher formation temperatures, as Co is often enriched in high-temperature pyrite generations (>300 °C; Metz and Trefry 2000). This is in good agreement with the mineralogical observations from pyrophyllite + illite samples at the NW Caldera that contain diaspore and zunyite indicating temperatures in excess of ~320 °C, minerals that are absent at the Upper Cone, suggesting lower fluid:rock ratios and higher fluid temperatures at the NW Caldera (de Ronde et al. 2019b,c). In addition to changes in trace metal content with age, the size and morphology of pyrite grains also varies. Pyrite at the younger Upper Cone site is generally euhedral, forms aggregates and is very fine-grained (<< 1 mm), whereas pyrite from the lower NW Caldera is coarse-grained and subhedral to anhedral (Fig. 3 and 4). This indicates a change in pyrite morphology with time due to recrystallization and in some cases, dissolution (Fig. 4L) related to prolonged exposure to high-temperature oxidized fluids (Fig. 12).

The similarity in trace metal enrichment signatures and sulfur isotope ratios between pyrite in pyrophyllite ± natroalunite alteration at the NW Caldera and Upper Cone with pyrite from overprinting chlorite + quartz-rich alteration (Fig. 5) indicates that pyrite is largely preserved during fluid overprinting, explaining the similar trace metal enrichment signature between all pyrite at Brothers. However, the relative depletion of pyrite from chlorite + quartz alteration in Cu, Te and Bi compared with all other pyrite indicates the remobilization of these metals during fluid overprinting at the NW Caldera and their subsequent deposition in black smoker chimneys at the seafloor (Berkenbosch et al. 2012, 2019). Our study provides evidence of metal remobilization from pyrite that, in addition to the scavenging of magmatic brines by seawater-derived hydrothermal fluids, is an important process in the accumulation of metals in hydrothermal precipitates at the seafloor at Brothers (de Ronde et al. 2019a). A later seawater overprint is absent at the Upper Cone, hence pyrite remains relatively enriched in Cu, Te and Bi compared to pyrite associated with chlorite + quartz alteration (Fig. 5A).

The enrichment of As, Sb, Ag, Pb and lower contents of Co, Se and Te in the shallow subsurface to ~30 mbsf in overprinting chlorite-rich alteration at the NW Caldera is best explained by seawater mixing during shallow recharge, although phase separation of the hydrothermal fluid cannot be ruled out. The absence of the same enrichment pattern with depth below the seafloor (Fig. 6) at the Upper Cone (Hole U1528D) indicates that fluid mixing and seawater recharge occurs over a much broader zone, supporting previous geophysical investigations that showed recharge of seawater through the Upper Cone walls and pit crater (Caratori-Tontini et al. 2012). In contrast, at the NW Caldera, ascending magmatic-hydrothermal fluid only undergoes high-degrees of mixing and cooling within ~30 m of the seafloor, causing a pronounced change in fluid temperature and the deposition of pyrite with a high As, Sb, Ag and Pb content.

Implications for formation of VMS and epithermal deposits

Data collected from below the seafloor at Brothers volcano offers a rare glimpse into subsurface processes in an active seafloor hydrothermal system. Brothers provides an analogue characterizing the transition between two major ore forming environments: volcanogenic massive sulfide (VMS) and high-sulfidation epithermal Au deposits (Sillitoe et al. 1996). At both the NW Caldera and Upper Cone sites metal enrichment below the seafloor is minimal, and only rarely were sulfide minerals other than pyrite observed. The low trace metal content of pyrite and absence of chalcopyrite and sphalerite, which are common in hydrothermal precipitates at the seafloor (Hannington et al. 2005), shows that mineralization containing high metal contents (i.e. several wt.% Zn or Cu), at least in the case of Brothers, is limited to a thin veneer at or near the seafloor, with sphalerite only commonly observed up to 30 mbsf. This shows that the potential to form economic mineralization below the seafloor is limited in both immature epithermal-type environments such as the Upper Cone and seawater-influenced systems like the NW Caldera. However, deposits that display transitional characteristics between seawater and magmatic-influenced systems, containing both pyrophyllite-rich and chlorite-rich alteration are prospective for mineral exploration due to the remobilization of metals from magmatic brines and overprinting of early pyrite generations that ultimately lead to the formation of metal-rich hydrothermal precipitates at the seafloor. Similar advanced-argillic alteration mineral assemblages have been documented in VMS deposits (Huston et al. 2011) such as LaRonde Penna (Canada; Mercier-Langevin et al. 2007), Mount Lyell (Tasmania; Large et al. 1996) and Boliden (Sweden; Mercier-Langevin et al. 2013). Understanding the transition from magmatic to seawater-influenced hydrothermal systems is important as LaRonde Penna, Mount Lyell and Boliden are all enriched in Au and classified as auriferous (Mercier-Langevin et al. 2011). The enrichment of Au in these deposits and associated advanced argillic alteration assemblage is attributed to the contribution of magmatic volatiles (Huston et al. 2011), hence characterizing the transition from magmatic to seawater-dominated hydrothermal systems is important for understanding the enrichment of Au in VMS deposits.

Summary and Conclusions

The combination of sulfur isotope and trace metal analysis of pyrite from below the seafloor at Brothers volcano shows variation with depth below the seafloor and between the NW Caldera and Upper Cone sites. Most trace metals occur in low concentrations and are incorporated in pyrite as a lattice bound substitution, with the exception of Zn, and more rarely Cu, which are hosted as micro-inclusions of sphalerite and chalcopyrite. Initially pyrite at the Upper Cone is enriched in Cu, As, Sb, Pb and Pt compared with older pyrite from pyrophyllite + illite alteration in the lower portion of the NW Caldera (<189 mbsf), which has a higher Cu, Te, Se and Bi content. This indicates a change in the trace metal content of pyrite with the age of the hydrothermal system related to higher fluid temperatures and prolonged exposure to magmatic volatile degassing.

The sulfur isotopic composition ($\delta^{34}S$) of pyrite supports previous interpretations that disproportionation of degassing SO_2 is a major source of sulfur in the Brothers hydrothermal system(s). In addition to SO_2 disproportionation, the occurrence of several values that are >0‰ at the NW Caldera indicates an additional source of sulfur, from TSR of seawater and leaching of host rocks. In combination, the uniform $\delta^{34}S$ composition and trace metal enrichment signature of pyrite across all alteration types indicate that pyrite did not undergo complete dissolution during seawater overprinting, although Cu, Te and Bi were remobilized by this process. These metals are then enriched in metal-sulfide-rich chimneys on the seafloor at the NW Caldera, further supporting the critical role of seawater-derived hydrothermal fluids in the formation of metal-rich hydrothermal precipitates at the seafloor.

Acknowledgments

This research used samples and data provided by the International Ocean Discovery Program (IODP). We thank the captain, crew and technical staff aboard the D/V *JOIDES Resolution* during Expedition 376 “Brothers Arc Flux”, May-July 5th, 2018. AJM acknowledges the support of the European Consortium for Ocean Research Drilling during his participation on Expedition 376. Post-cruise research was funded by the Natural Environmental Research Council grant NE/S006214/1 awarded to CJM and AJM at Cardiff University. JWJ acknowledges support from the Canada Research Chair program. CdR acknowledges funding from the Ministry of Business, Innovation and Employment of the New Zealand Government. We thank S. Tombros and an anonymous reviewer for their valuable feedback and associate editor D. Zhai and editor-in-chief G. Beaudoin for the editorial handling of this manuscript.

Author contributions

AJM was responsible for the study conception and design. Material preparation, data collection and analysis were performed by AJM, GP and IMD. The first draft of the manuscript was written by AJM and all authors commented on previous versions of the manuscript. All authors read and approved the final manuscript.

References

Abraitis PK, Pattrick RAD, Vaughan DJ (2004) Variations in the compositional, textural and electrical properties of natural pyrite: a review. International Journal of Mineral Processing 74, 41–59.

Baker ET, Walker SL, Embley RW, de Ronde CEJ (2012) High-Resolution Hydrothermal Mapping of Brothers Caldera, Kermadec Arc. Econ Geol 107:1583–1593

Banerjee NR, Gillis KM, Muehlenbachs K (2000) Discovery of epidosites in a modern oceanic setting, the Tonga forearc. Geology 28:151-154

Berkenbosch HA, de Ronde CEJ, Ryan CG, McNeill AW, Howard DL, Gemmell JB, Danyushevsky LV (2019) Trace Element Mapping of Copper- and Zinc-Rich Black Smoker Chimneys from Brothers Volcano, Kermadec Arc, Using Synchrotron Radiation XFM and LA-ICP-MS. Econ Geol 114:67–92

Berkenbosch HA, de Ronde CEJ, Gemmell JB, McNeill AW, Goemann K (2012) Mineralogy and Formation of Black Smoker Chimneys from Brothers Submarine Volcano, Kermadec Arc. Econ Geol 107:1613–1633

Binns RA, Barriga FJAS, Miller DJ, et al. (2002) *in* Binns RA. et al. eds., Initial report summary, Leg 193 Proceedings of the International Ocean Discovery Program: College Station, Texas, International Ocean Discovery Program, pp. 84

Brueckner SM, Piercey SJ, Layne GD, Piercey G, Sylvester PJ (2015) Variations of sulphur isotope signatures in sulphides from the metamorphosed Ming Cu(−Au) volcanogenic massive sulphide deposit, Newfoundland Appalachians, Canada. Miner Deposita 50:619–640

Butler IB, Nesbitt RW (1999) Trace element distributions in the chalcopyrite wall of a black smoker chimney: insights from laser ablation inductively coupled plasma mass spectrometry (LA–ICP–MS). Earth Planet Sci Lett 167:335–345

Butterfield DA, Nakamura K, Takano B, Lilley MD, Lupton JE, Resing JA, Roe KK (2011) High SO2 flux, sulfur accumulation, and gas fractionation at an erupting submarine volcano. Geology 39: 803–806

Caratori Tontini F, Tivey MA, de Ronde CEJ, Humphris SE (2019) Heat Flow and Near-Seafloor Magnetic Anomalies Highlight Hydrothermal Circulation at Brothers Volcano Caldera, Southern Kermadec Arc, New Zealand. Geophys Res Lett 46:8252–8260

Caratori Tontini F, de Ronde CEJ, Yoerger D, Kinsey J, Tivey M (2012) 3-D focused inversion of near-seafloor magnetic data with application to the Brothers volcano hydrothermal system, Southern Pacific Ocean, New Zealand. J Geophys Res Solid Earth 117:B10102

Cook NJ, Ciobanu CL, Pring A, Skinner W, Shimizu M, Danyushevsky L, Saini-Eidukat B, Melcher F (2009) Trace and minor elements in sphalerite: A LA-ICPMS study. Geochim Cosmochim Acta 73:4761–4791

de Ronde CEJ, Butterfield DA, Leybourne MI (2012) Metallogenesis and Mineralization of Intraoceanic Arcs I: Kermadec Arc—Introduction. Econ Geol p.107:1521–1525

de Ronde CEJ, Faure K, Bray CJ, Chappell DA, Wright IC (2003) Hydrothermal fluids associated with seafloor mineralization at two southern Kermadec arc volcanoes, offshore New Zealand. Miner Deposita 38:217–233 de Ronde CEJ, Chadwick WW, Ditchburn RG, Embley RW, Tunnicliffe V, Baker ET, Walker SL, Ferrini VL, Merle SM (2015) Molten Sulfur Lakes of Intraoceanic Arc Volcanoes, in: Rouwet, D., Christenson, B., Tassi, F., Vandemeulebrouck, J. (Eds.), Volcanic Lakes, Advances in Volcanology. Springer, Berlin, Heidelberg, pp. 261–288

de Ronde CEJ, Massoth GJ, Butterfield DA, Christenson BW, Ishibashi J, Ditchburn RG, Hannington MD, Brathwaite RL, Lupton JE, Kamenetsky VS, Graham IJ, Zellmer GF, Dziak RP, Embley RW, Dekov VM, Munnik F, Lahr J, Evans LJ, Takai K (2011) Submarine hydrothermal activity and gold-rich mineralization at Brothers Volcano, Kermadec Arc, New Zealand. Miner Deposita 46:541–584

de Ronde CEJ, Hannington MD, Stoffers P, Wright IC, Ditchburn RG, Reyes AG, Baker ET, Massoth GJ, Lupton JE, Walker SL, Greene RR, Soong CWR, Ishibashi J, Lebon GT, Bray CJ, Resing JA (2005) Evolution of a Submarine Magmatic-Hydrothermal System: Brothers Volcano, Southern Kermadec Arc, New Zealand. Econ Geol 100:1097–1133

de Ronde CEJ, Humphris SE, Höfig TW, Reyes AG (2019a) Critical role of caldera collapse in the formation of seafloor mineralization: The case of Brothers volcano. Geology 47:762–766

de Ronde CEJ, Humphris SE, Höfig TW, and the Expedition 376 Scientists (2019b) Site U1528, *in* de Ronde CEJ, et al. (ed.), Brothers Arc Flux: Proceedings of the International Ocean Discovery Program, Volume 376: College Station, Texas, International Ocean Discovery Program, 66 p.

de Ronde CEJ, Humphris SE, Höfig TW, and the Expedition 376 Scientists (2019b) Site U1530, *in* de Ronde CEJ, et al. (ed.), Brothers Arc Flux: Proceedings of the International Ocean Discovery Program, Volume 376: College Station, Texas, International Ocean Discovery Program, 53 p.

Deditius AP, Reich M, Kesler SE, Utsunomiya S, Chryssoulis SL, Walshe J, Ewing RC (2014) The coupled geochemistry of Au and As in pyrite from hydrothermal ore deposits. Geochim Cosmochim Acta 140:644–670

Deditius AP, Utsunomiya S, Reich M, Kesler SE, Ewing RC, Hough R, Walshe J (2011) Trace metal nanoparticles in pyrite. Ore Geol Rev 42:32–46

Diehl A, de Ronde CEJ, Bach W (2020) Subcritical Phase Separation and Occurrence of Deep-Seated Brines at the NW Caldera Vent Field, Brothers Volcano: Evidence from Fluid Inclusions in Hydrothermal Precipitates. Geofluids 8868259

Ditchburn RG, de Ronde CEJ (2017) Evidence for Remobilization of Barite Affecting Radiometric Dating Using 228Ra, 228Th, and 226Ra/Ba Values: Implications for the Evolution of Sea-Floor Volcanogenic Massive Sulfides. Econ Geol 112:1231–1245

Edmonds HN, German CR, Green DRH, Huh Y, Gamo T, Edmond JM (1996) Continuation of the hydrothermal fluid chemistry time series at TAG, and the effects of ODP drilling. Geophys Resh Lett 23:3487–3489

Edmonds M, Wallace PJ (2017) Volatiles and Exsolved Vapor in Volcanic Systems. Elements 13:29–34

Embley RW, de Ronde CEJ, Merle SG, Davy B, Caratori Tontini F (2012) Detailed Morphology and Structure of an Active Submarine Arc Caldera: Brothers Volcano, Kermadec Arc. Econ Geol 107:1557–1570.

Fuchs S, Hannington MD, Petersen S (2019) Divining gold in seafloor polymetallic massive sulfide systems. Miner Deposita 54:789–820

Fouquet Y, Zierenberg RA, Miller DJ and Leg 169 Scientists (1998). , Fouquet et al. (ed.), Initial reports of the Ocean Drilling Program, Leg 169: College Station, Texas, Ocean Drilling Program, p. 205-252

Gemmell JB, Sharpe R, Jonasson IR, Herzig PM (2004) Sulfur Isotope Evidence for Magmatic Contributions to Submarine and Subaerial Gold Mineralization: Conical Seamount and the Ladolam Gold Deposit, Papua New Guinea. Econ Geol 99:1711–1725

George LL, Cook NJ, Ciobanu CL (2016) Partitioning of trace elements in co-crystallized sphalerite–galena–chalcopyrite hydrothermal ores. Ore Geol Rev 77:97–116

Giggenbach WF (1996) Chemical Composition of Volcanic Gases, in: Scarpa, R., Tilling, R.I. (Eds.), Monitoring and Mitigation of Volcano Hazards. Springer, Berlin, Heidelberg, pp. 221–256

Goldschmidt VM, Muir A (1954) Geochemistry. Clarendon Press, Oxford, p. 730

Grant HLJ, Hannington MD, Petersen S, Frische M, Fuchs SH (2018) Constraints on the behavior of trace elements in the actively-forming TAG deposit, Mid-Atlantic Ridge, based on LA-ICP-MS analyses of pyrite. Chem Geol 498:45–71

Gruen G, Weis P, Driesner T, Heinrich CA, de Ronde CEJ (2014) Hydrologic controls on different styles of magmatic-hydrothermal activity with implications for ore deposit formation at submarine arc volcanoes. Earth Planet Sci Lett 404:307-318

Haase KM, Stroncik N, Garbe-Schönberg D, Stoffers P (2006) Formation of island arc dacite magmas by extreme crystal fractionation: An example from Brothers Seamount, Kermadec island arc (SW Pacific). J Volcanol Geotherm Res 152, 316-330

Hannington MD, Tivey MK, Larocque ACL, Petersen S, Rona PA (1995) The occurrence of gold in sulfide deposits of the TAG hydrothermal field, Mid-Atlantic Ridge. Canad Mineral33:1285–1310

Hannington MD, de Ronde CEJ, Petersen S (2005) Sea-floor tectonics and submarine hydrothermal systems, in: Hedenquist, J.W., Thompson, J.F.H., Goldfarb, R.J., Richards, J.P. (ed.), Economic Geology 100th Anniversary Volume. Society of Economic Geologists, Littelton, Colorado, USA, pp. 111–141

Hedenquist JW, Lowenstern JB (1994) The role of magmas in the formation of hydrothermal ore deposits. Nature 370:519–527

Herzig PM, Hannington MD, Arribas A (1998) Sulfur isotopic composition of hydrothermal precipitates from the Lau back-arc: implications for magmatic contributions to seafloor hydrothermal systems. Miner Deposita 33:226–237

Humphris SE, Herzig P, Miller D (1996) Introduction and principal results, in Humphris SE, et al. (ed.) Proceeding of the Ocean Drilling Program Initial Reports, Volume 158: College Station, Texas, International Ocean Discovery Program, 14 p.

Humphris SE, Herzig PM, Miller DJ, Alt JC, Becker K, Brown D, Brügmann G, Chiba H, Fouquet Y, Gemmell JB, Guerin G, Hannington MD, Holm NG, Honnorez JJ, Iturrino GJ, Knott R, Ludwig R, Nakamura K, Petersen S, Reysenbach A-L, Rona PA, Smith AAS, Tivey MK, Zhao X (1995) The internal structure of an active sea-floor massive sulphide deposit. Nature 377:713–716

Humphris SE, Thompson G (1978) Trace element mobility during hydrothermal alteration of oceanic basalts. Geoch Cosmochim Acta 42:127–136

Huston DL, Relvas JMRS, Gemmell JB, Drieberg S (2011) The role of granites in volcanic-hosted massive sulphide ore-forming systems: an assessment of magmatic–hydrothermal contributions. Miner Deposita 46:473–507

Huston DL, Sie SH, Suter GF, Cooke DR, Both RA (1995) Trace elements in sulfide minerals from eastern Australian volcanic-hosted massive sulfide deposits; Part I, Proton microprobe analyses of pyrite, chalcopyrite, and sphalerite, and Part II, Selenium levels in pyrite; comparison with delta 34 S values and implications for the source of sulfur in volcanogenic hydrothermal systems. Econ Geol 90:1167–1196

Keith M, Haase KM, Klemd R, Smith DJ, Schwarz-Schampera U, Bach W (2018b) Constraints on the source of Cu in a submarine magmatic-hydrothermal system, Brothers volcano, Kermadec island arc. Contrib Mineral Petrol 173-40:1-16

Keith M, Häckel F, Haase KM, Schwarz-Schampera U, Klemd R (2016) Trace element systematics of pyrite from submarine hydrothermal vents. Ore Geol Rev 72:728–745

Keith M, Smith DJ, Jenkin GRT, Holwell DA, Dye MD (2018a) A review of Te and Se systematics in hydrothermal pyrite from precious metal deposits: Insights into ore-forming processes. Ore Geol Rev 96:269–282

Kleint C, Bach W, Diehl A, Fröhberg N, Garbe-Schönberg D, Hartmann JF, de Ronde CEJ, Sander SG, Strauss H, Stucker VK, Thal J, Zitoun R, Koschinsky A (2019) Geochemical characterization of highly diverse hydrothermal fluids from volcanic vent systems of the Kermadec intraoceanic arc. Chem Geol 528:119289

Kusakabe M, Komoda Y, Takano B, Abiko T (2000) Sulfur isotopic effects in the disproportionation reaction of sulfur dioxide in hydrothermal fluids: implications for the δ34S variations of dissolved bisulfate and elemental sulfur from active crater lakes. J Volcanol Geotherm Res 97:287–307

Large RR (1992) Australian volcanic-hosted massive sulfide deposits: features, styles, and genetic models. Econ Geol 87:471–510

Large RR, Danyushevsky L, Hollit C, Maslennikov V, Meffre S, Gilbert S, Bull S, Scott R, Emsbo P, Thomas H, Singh B, Foster J (2009) Gold and Trace Element Zonation in Pyrite Using a Laser Imaging Technique: Implications for the Timing of Gold in Orogenic and Carlin-Style Sediment-Hosted Deposits. Econ Geol 104:635–668

Large RR, Doyle M, Raymond O, Cooke D, Jones A, Heasman L (1996) Evaluation of the role of Cambrian granites in the genesis of world class VHMS deposits in Tasmania. Ore Geol Rev, 10:215-230

Layton-Matthews D, Leybourne MI, Peter JM, Scott SD, Cousens B, Eglington BM (2013) Multiple sources of selenium in ancient seafloor hydrothermal systems: Compositional and Se, S, and Pb isotopic evidence from volcanic-hosted and volcanic-sediment-hosted massive sulfide deposits of the Finlayson Lake District, Yukon, Canada. Geochim Cosmochim Acta 117:313-331

Martin AJ, Keith M, Parvaz DB, McDonald I, Boyce AJ, McFall KA, Jenkin GRT, Strauss H, MacLeod CJ (2020) Effects of magmatic volatile influx in mafic VMS hydrothermal systems: Evidence from the Troodos ophiolite, Cyprus. Chem Geol 531:119325

Martin AJ, McDonald I, Jenkin GRT, McFall KA, Boyce AJ, Jamieson JW, MacLeod CJ (2021) A missing link between ancient and active mafic-hosted seafloor hydrothermal systems – Magmatic volatile influx in the exceptionally preserved Mala VMS deposit, Troodos, Cyprus. Chem Geol 567:120127

Martin AJ, Jamieson JW, de Ronde CEJ, Humphris SE, Roberts S, Macleod CJ, Cai Y, Zhang C, Schlicht LEM, Nozaki T (2022). Hydrothermal alteration within the Brothers submarine arc volcano, Kermadec arc, New Zealand. Econ Geol. https://doi.org/10.5382/econgeo.4962

Maslennikov VV, Maslennikova SP, Large RR, Danyushevsky LV (2009) Study of Trace Element Zonation in Vent Chimneys from the Silurian Yaman-Kasy Volcanic-Hosted Massive Sulfide Deposit (Southern Urals, Russia) Using Laser Ablation-Inductively Coupled Plasma Mass Spectrometry (LA-ICPMS). Econ Geol 104:1111–1141

McDermott JM, Ono S, Tivey MK, Seewald JS, Shanks WC, Solow AR (2015) Identification of sulfur sources and isotopic equilibria in submarine hot-springs using multiple sulfur isotopes. Geochim Cosmochim Acta 160:169–187

Melekestseva IY, Tret'yakov GA, Nimis P, Yuminov AM, Maslennikov VV, Maslennikova SP, Kotlyarov VA, Beltenev VE, Danyushevsky LV, Large RR (2014) Barite-rich massive sulfides from the Semenov-1 hydrothermal field (Mid-Atlantic Ridge, 13°30.87′ N): Evidence for phase separation and magmatic input. Mar Geol 349:37–54

Mercier-Langevin P, Dubé B, Hannington MD, Davis DW, Lafrance B, Gosselin G (2007) The LaRonde Penna Au-Rich Volcanogenic Massive Sulfide Deposit, Abitibi Greenstone Belt, Quebec: Part I. Geology and Geochronology. Econ Geol 102: 585–609

Mercier-Langevin P, Hannington MD, Dubé B, Bécu V (2011) The gold content of volcanogenic massive sulfide deposits. Miner Deposita 46, 509–539

Mercier-Langevin P, McNicoll V, Allen RL, Blight JHS, Dubé B (2013) The Boliden gold-rich volcanogenic massive sulfide deposit, Skellefte district, Sweden: new U–Pb age constraints and implications at deposit and district scale. Miner Deposita 48, 485–504

Metz S, Trefry JH (2000) Chemical and mineralogical influences on concentrations of trace metals in hydrothermal fluids. Geochim Cosmochim Acta 64:2267–2279

Monecke T, Petersen S, Hannington MD, Grant H, Samson I (2016) The minor element endowment of modern sea-floor massive sulfide deposits and comparison with deposits hosted in ancient volcanic successions, in: Verplanck, P.L., Hitzman, M.W. (ed.), Rare Earth and Critical Elements in Ore Deposits. Society of Economic Geologists, Knoxville, Tenn., pp. 245–306

Nestmeyer M, Keith M, Haase KM, Klemd R, Voudouris P, Schwarz-Schampera U, Strauss H, Kati M, Magganas A (2021) Trace Element Signatures in Pyrite and Marcasite From Shallow Marine Island Arc-Related Hydrothermal Vents, Calypso Vents, New Zealand, and Paleochori Bay, Greece. Front Earth Sci 9:138

Ohmoto H, Lasaga AC (1982) Kinetics of reactions between aqueous sulfates and sulfides in hydrothermal systems. Geochim Cosmochim Acta 46:1727–1745

Ono S, Shanks WC, Rouxel OJ, Rumble D (2007) S-33 constraints on the seawater sulfate contribution in modern seafloor hydrothermal vent sulfides. Geochim Cosmochim Acta 71:1170–1182

Patten CGC, Pitcairn IK, Alt JC, Zack T, Lahaye Y, Teagle DAH, Markdahl K (2020) Metal fluxes during magmatic degassing in the oceanic crust: sulfide mineralisation at ODP site 786B, Izu-Bonin forearc. Mineral Deposita 55:469–489

Peters C, Strauss H, Haase K, Bach W, de Ronde CEJ, Kleint C, Stucker V (2021) SO2 disproportionation impacting hydrothermal sulfur cycling: Insights from multiple sulfur isotopes for hydrothermal fluids from the Tonga-Kermadec intraoceanic arc and the NE Lau Basin. Chem Geol 120586.

Petersen S, Herzig PM, Hannington MD, Jonasson IR, Arribas A (2002) Submarine Gold Mineralization Near Lihir Island, New Ireland Fore-Arc, Papua New Guinea. Economic Geology 97, 1795–1813.

Prichard HM, Knight RD, Fisher PC, McDonald I, Zhou MF, Wang CY (2013) Distribution of platinum-group elements in magmatic and altered ores in the Jinchuan intrusion, China: an example of selenium remobilization by postmagmatic fluids. Miner Deposita 48:767–786

Rahm M, Hoffmann R, Ashcroft NW (2016) Atomic and Ionic Radii of Elements 1–96. Chem Eur J 22: 14625–14632

Rees CE, Jenkins WJ, Monster J (1978) The sulphur isotopic composition of ocean water sulphate. Geochim Cosmochim Acta 42:377–381

Reich M, Kesler SE, Utsunomiya S, Palenik CS, Chryssoulis SL, Ewing RC (2005). Solubility of gold in arsenian pyrite. Geochim Cosmochim Acta 69:2781–2796

Reyes AG (1990) Petrology of Philippine geothermal systems and the application of alteration mineralogy to their assessment. J Volcanol Geotherm Res 43:279–309

Richardson CJ, Cann JR, Richards HG, Cowan JG (1987) Metal-depleted root zones of the Troodos ore-forming hydrothermal systems, Cyprus. Earth Plan Sci Lett 84:243–253

Ryan WBF, Carbotte SM, Coplan JO, O'Hara S, Melkonian A, Arko R, Weissel RA, Ferrini V, Goodwillie A, Nitsche F, Bonczkowski J, Zemsky R (2009) Global Multi-Resolution Topography synthesis, Geochem Geophys Geosyst 10:Q03014

Sakai H (1968) Isotopic properties of sulfur compounds in hydrothermal processes. Geochem J 2:29–49

Sakai H, Marais DJD, Ueda A, Moore JG (1984) Concentrations and isotope ratios of carbon, nitrogen and sulfur in ocean-floor basalts. Geochim Cosmochim Acta 48:2433–2441

Sillitoe RH, Hannington MD, Thompson JFH (1996) High sulfidation deposits in the volcanogenic massive sulfide environment. Econ Geol 91:204–212

Stucker VK, de Ronde CEJ, Laurence KJ, Phillips AM (2022) Rare Time Series of Hydrothermal Fluids for a Submarine Volcano: 14 Years of Vent Fluid Compositions for Brothers Volcano, Kermadec Arc New Zealand. Econ Geol https://doi.org/10.5382/econgeo.4922

Takai K, Mottl MJ, Nielsen SH and the Expedition 331 Scientists (2011) Proceedings of the International Ocean Discovery Program, Volume 331: College Station, Texas, International Ocean Discovery Program, p. 39

Timm C, de Ronde CEJ, Leybourne MI, Layton-Matthews D, Graham IJ (2012) Sources of Chalcophile and Siderophile Elements in Kermadec Arc Lavas. Econ Geol 107:1527–1538

Tivey MK, Humphris SE, Thompson G, Hannington MD, Rona PA (1995) Deducing patterns of fluid flow and mixing within the TAG active hydrothermal mound using mineralogical and geochemical data. J Geophys Res: Solid Earth 100:12527–12555

Wallace PJ (2005) Volatiles in subduction zone magmas: concentrations and fluxes based on melt inclusion and volcanic gas data. J Volcanol Geotherm Res 140:217–240

Wohlgemuth-Ueberwasser CC, Viljoen F, Petersen S, Vorster C (2015) Distribution and solubility limits of trace elements in hydrothermal black smoker sulfides: An in-situ LA-ICP-MS study. Geochim Cosmochim Acta 159:16–41

Wright IC, Gamble JA (1999) Southern Kermadec submarine caldera arc volcanoes (SW Pacific): caldera formation by effusive and pyroclastic eruption. Mar Geol 161:207–227

Wysoczanski RJ, Handler MR, Schipper CI, Leybourne MI, Creech J, Rotella MD, Nichols ARL, Wilson CJN, Stewart RB (2012) The Tectonomagmatic Source of Ore Metals and Volatile Elements in the Southern Kermadec Arc. Econ Geol 107:1539–1556

Yang K, Scott SD (2002) Magmatic Degassing of Volatiles and Ore Metals into a Hydrothermal System on the Modern Sea Floor of the Eastern Manus Back-Arc Basin, Western Pacific. Econ Geol 97: 1079–1100

Yang K, Scott SD (1996) Possible contribution of a metal-rich magmatic fluid to a sea-floor hydrothermal system. Nature 383:420–423

Yeats CJ, Parr JM, Binns RA, Gemmell JB, Scott SD (2014) The SuSu Knolls Hydrothermal Field, Eastern Manus Basin, Papua New Guinea: An Active Submarine High-Sulfidation Copper-Gold System. Econ Geol 109:2207–2226

Zeng Z, Liu C, Chen CA, Yin X, Chen D, Wang XY, Wang X, Zhang G (2007) Origin of a native sulfur chimney in the Kueishantao hydrothermal field, offshore northeast Taiwan. Sci China Earth Sci 50:1746-1753

Figure Captions

Figure 1: Location map of Kermadec-Tonga arc and surrounding area. Brothers volcano is located on the southern Kermadec arc, NE of New Zealand (data: http://www.geomapapp.org; Ryan et al. 2009)

Figure 2: Bathymetric map of Brothers volcano. A) Approximate location of drill sites investigated in this study. Hole U1530A is located at the NW Caldera site and Hole U1528D is located at the Upper Cone (legend as in image B). B) 3D visualization of Brothers caldera looking approximately NE, note that the bathymetry is exaggerated by 2 times (data: GNS Science).

Figure 3: Representative photographs of drill core sections and photomicrographs of pyrite in reflected light from the NW Caldera site. A-1) Core recovery (black lines) and the distribution of different alteration mineral assemblages with depth below the seafloor (green = chlorite-rich, red = pyrophyllite-rich). A) Stockwork veins from 26 mbsf containing pyrite + barite + anhydrite ± sphalerite (core section 5R1, 25.9 mbsf). Clast material consists of smectite + chlorite + quartz. B) Brecciated sample (core section 13R1, 64.3 mbsf) containing chlorite + quartz altered clasts with a matrix of pyrite + quartz + anhydrite. C) Representative sample of pyrophyllite + illite alteration (core section 48R1, 232.3 mbsf). Light coloured regions are quartz + anhydrite-rich whereas buff-beige areas are illite + pyrophyllite-rich. D) Anhydrite + pyrite vein containing coarse subhedral-to-euhedral pyrite (core section 1R1, 0.3 mbsf). E) Subhedral to euhedral pyrite from chlorite + quartz alteration zone (core section 69R1, 333.2 mbsf). F) Fine-grained euhedral pyrite aggregates in a matrix of chlorite + quartz (core section 5R1, 25.9 mbsf). G) Pyrite in

pyrophyllite + illite alteration associated with a late, cross-cutting anhydrite vein (core section 44R1, 214.0 mbsf). H) Subhedral pyrite grains with abundant sphalerite inclusions (inset image) from pyrophyllite + illite alteration zone (core section 65R1, 314.4 mbsf). I) Anhedral, resorbed pyrite from pyrophyllite + illite alteration zone (core section 69R1, 333.2 mbsf). J) Euhedral pyrite with radial zonations delineating multiple generations of overgrowth (core section 1R1, 0.3 mbsf). K) Subhedral pyrite from chlorite + quartz alteration with weak zonation and a relict core "C" indicating recrystallization. White dashed lines delineate relict crystal faces (core section 89R1, 429. 5 mbsf). Inset image provides a close up view of an area with chaotic zonations with grain boundaries delineated by brighter orange colors. L) Anhedral pyrite with radial zonations that are subparallel to the grain margin showing a prominent relict core "C" zone (core section 65R1, 314.4 mbsf). Images J to L have been etched for 90 s with NaOCl. Sample intervals and depths in ESM 1, Table T2.

Figure 4: Representative photographs of drill sections and photomicrographs of pyrite grains in reflected light from the Upper Cone site. A-1) Core recovery (black lines) and the distribution of different alteration mineral assemblages with depth below the seafloor (blue = smectite-rich, pink = natroalunite + pyrophyllite-rich, orange = natrolaunite-rich). A) Natroalunite bearing alteration containing bleached selvages (white material) with native sulfur (Nat S) infilling porosity (core section 18R2, 138.9 mbsf). B) Natroalunite + pyrophyllite alteration with a prominent brecciated texture; clasts (C) are variably altered with their rim often appearing more altered than the core (core section 9R1, 95.1 mbsf). C) Smectite-rich alteration containing primary plagioclase (core section 37R1, 229.7 mbsf). D) Fine-grained subhedral to euhedral pyrite in a matrix of pyrophyllite + quartz (core section 6R1, 85.6 mbsf). E) Pyrite associated with a cross-cutting anhydrite veinlet (core section 5R2, 77.6 mbsf). F) Pyrite surrounding a plagioclase glomerocryst that has been replaced by natroalunite + anhydrite (core section 55R1, 316.7 mbsf). G) Pyrite associated with anhydrite that has replaced a plagioclase + pyroxene glomerocryst (core section 14R1, 120.2 mbsf). H) An aggregate of euhedral pyrite infilling porosity (core section 11R3, 104.9 mbsf). I) Fine-grained euhedral pyrite associated with secondary Ti minerals (core section 9R1, 95.4 mbsf). J) Euhedral

to subhedral pyrite with sub-grains with no internal zonation (core section, 5R1 75.7 mbsf). K) An aggregate of very fine-grained pyrite with some grains exhibiting radial zonation (core section 11R3, 104.9 mbsf). L) Very fine-grained pyrite exhibiting parallel zonation and an inclusion-rich core (core section 38R1, 234.5 mbsf). Images J to L have been etched for 90 s with NaOCl. Sample intervals available in ESM 1, Table T2.

Figure 5: Trace metal geochemistry of pyrite (LA-ICP-MS) classified by alteration mineralogy. A) Comparison of the median concentration of trace metals in pyrite from natroalunite (N-alun, *n= 37 spots*), natroalunite + pyrophyllite (N-alun + prl, *n= 151 spots*), smectite + plagioclase (smec + plag, *n= 28 spots*), pyrophyllite + illite (prl + ill, *n= 76 spots*) and chlorite + quartz (chl + qtz, *n=53 spots*) alteration. The grey line represents the median trace metal content for all pyrite and the surrounding grey area is the interquartile range. All pyrite exhibits broadly the same trace metal signature but the absolute abundance of different metals varies, notably pyrite from chlorite + quartz alteration is relatively depleted in Cu, Te and Bi. B) Cu, C) Zn, D) Pb, E) Co, F) As, G) Se, H) Te, I) Sb, J) Ag, K) Pt, L) Au, M) Bi.

Figure 6: Variation in downhole trace metal contents of pyrite from A) the NW Caldera site and B) the Upper Cone site for Co, Cu, Se, Te, Bi, Sb, Pb, As and Ag. In Hole U1530A at the NW Caldera site, Sb, Pb, As and Ag are enriched near the seafloor in chlorite-rich alteration. In Hole U1528D at the Upper Cone site, most trace metals are enriched in samples above 153 mbsf relative to deeper samples. Black dots represent the median trace metal content of a given sample and error bars span the minimum and maximum contents.

Figure 7: Sulfur isotope composition ($\delta^{34}S$) of pyrite from the NW Caldera (red and green) and Upper Cone (orange, pink blue) sites, classified by alteration mineralogy (N-alun *n= 8*, N-alun + prl, *n= 16*, Smec + plag *n= 7*, Prl + ill *n= 20*, chl + qtz *n*= 27). The median $\delta^{34}S$ value for all alteration types is similar. Data available in ESM 1, Table T7.

Figure 8: Downhole variations in the sulfur isotope composition ($\delta^{34}S$) of pyrite. A) Average $\delta^{34}S$ values in pyrite from Hole U1530A of the NW Caldera (*n= 46 points,* 14 samples). B) Average $\delta^{34}S$ values in pyrite from Hole U1528D of the Upper Cone site (*n= 32 points*, 13 samples). Error bars represent minimum and maximum value for a given sample. Vent fluid HS^- (de Ronde et al. 2011) and arc-enriched mantle (McDermott et al. 2015).

Figure 9: Representative time resolved analysis (TRA) (LA-ICP-MS) for pyrite (counts per second vs. time). A smooth ablation profile indicates the incorporation of trace metals in a solid solution, or as nano-scale inclusions, whereas a jagged profile typically indicates mineral inclusions (note logarithmic scale). A) Pyrite from core section 52R2 (301.7 mbsf, Hole U1528D). B) Pyrite from core section 29R2 (191.3 mbsf, Hole U1528D) contains inclusions of probable sphalerite (sph) and chalcopyrite (ccp). Grey box marks gas blank measurement. Red arrow = laser off.

Figure 10: Geochemical discrimination diagrams for pyrite geochemistry. Data from this study are indicated by the colored symbols and are classified based on alteration mineralogy. Gray symbols are the LA-ICP-MS analysis of pyrite from other seafloor massive sulfide deposits. A) Au vs. As. The black dashed line marks the solubility limit of Au in pyrite as a function of As concentration. Concentrations below the solid black dashed line are considered to be hosted in a lattice bound solid solution whereas values above indicate inclusions (after Reich et al. 2005). B) Te vs. As. The black dashed line indicates the maximum solubility of Te as a function of As concentration. Points that plot above the line indicate the occurrence of inclusions (after Keith et al. 2018a). C) Sb vs. As, samples from the NW Caldera site are notably enriched in Sb and As. D) Boiling discrimination plot using the ratio of Sb/Pb and Bi/Pb (after Román et al. 2019). All data in ppm. Gray symbols are the LA-ICP-MS analysis of pyrite from other seafloor massive sulfide deposits (de Ronde et al. 2011 – whole rock data; Wohlgemuth-Ueberwasser et al. 2015; Keith et al. 2016; Grant et al. 2018).

Figure 11: Summary of sulfur isotope composition of sulfide minerals from Brothers. The average $\delta^{34}S$ composition of sulfide minerals, native sulfur and vent fluid HS (data from de Ronde et al. 2003, 2005, 2011).

Figure 12: Summary of pyrite evolution, trace metal enrichment signatures and sulfur isotope composition of sub-seafloor pyrite at the Brothers volcano. A) Pyrite forming at the Upper Cone site. Pyrite is fine-grained, euhedral and enriched in Cu, As, Sb and Pb. Disproportionation of degassing SO_2 is the primary source of sulfur. B) Pyrite from pyrophyllite + illite alteration at the NW Caldera. Pyrite becomes progressively coarser due to recrystallization with time and is relatively enriched in Co, Se, Te and Bi with a subhedral grain morphology. Cobalt, Se, Te and Bi are progressively enriched due to prolonged periods of magmatic volatile degassing at high-temperature (>300 °C). C) Seawater-derived hydrothermal overprinting of pyrophyllite + illite alteration and the formation of chlorite + quartz alteration at the NW Caldera. Hydrothermal fluids remobilize Cu, Te and Bi from pyrite but the trace metal enrichment signature and $\delta^{34}S$ value remains unchanged, indicating that pyrite did not undergo complete dissolution during fluid overprinting.

Table Captions

Table 1: Summary of pyrite trace metal contents from the NW Caldera and Upper Cone site, classified by alteration mineral assemblage. Av. = average, med. = median, σ = one standard deviation, max = maximum. Chl + qtz = chlorite + quartz, Prl + ill = pyrophyllite + illite, Smec + plg = smectite + plagioclase, N-alu + prl = natroalunite + pyrophyllite, N-alu = natrolaunite (ESM 1, Table T4 and 5).

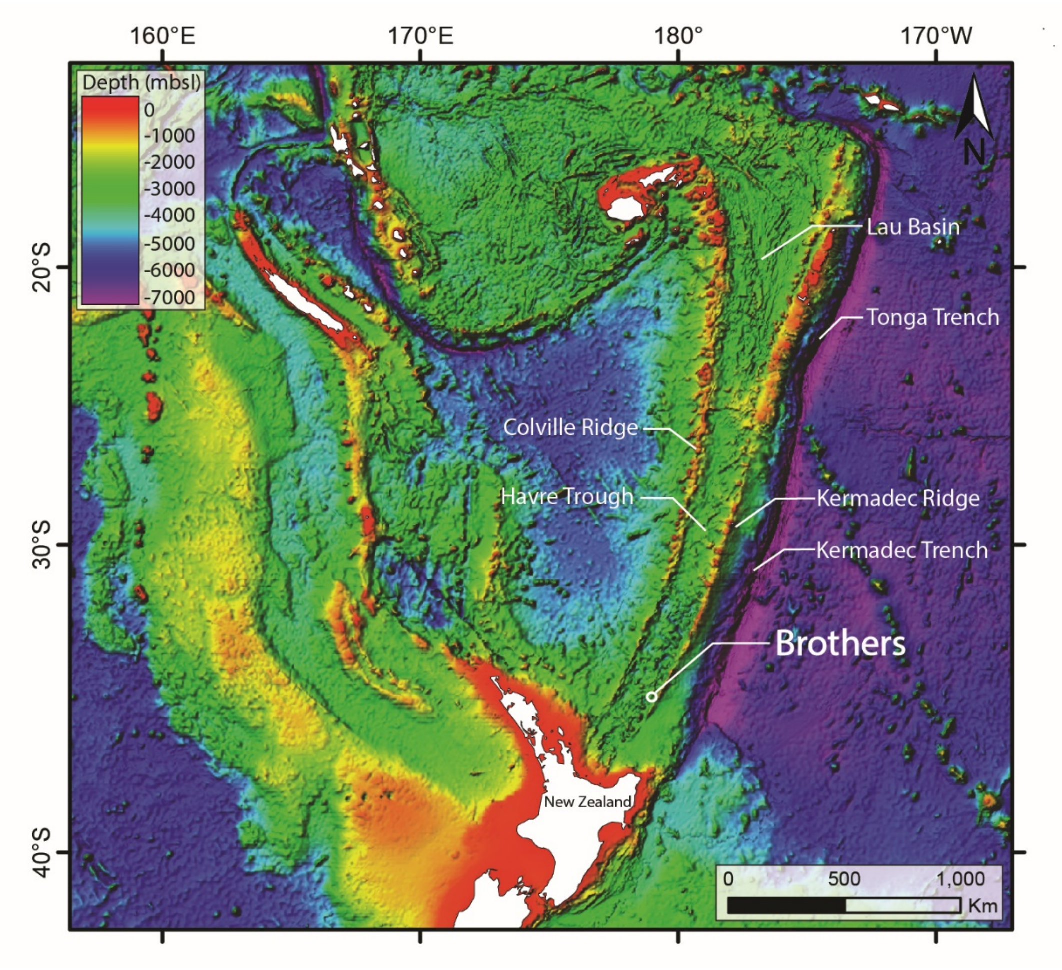
160°E
170°E
180°
170°W
20°S
30°S
40°S
Depth (mbsl)
0
-1000
-2000
-3000
-4000
-5000
-6000
-7000
N
Lau Basin
Tonga Trench
Colville Ridge
Havre Trough
Kermadec Ridge
Kermadec Trench
Brothers
New Zealand
0
500
1,000
Km

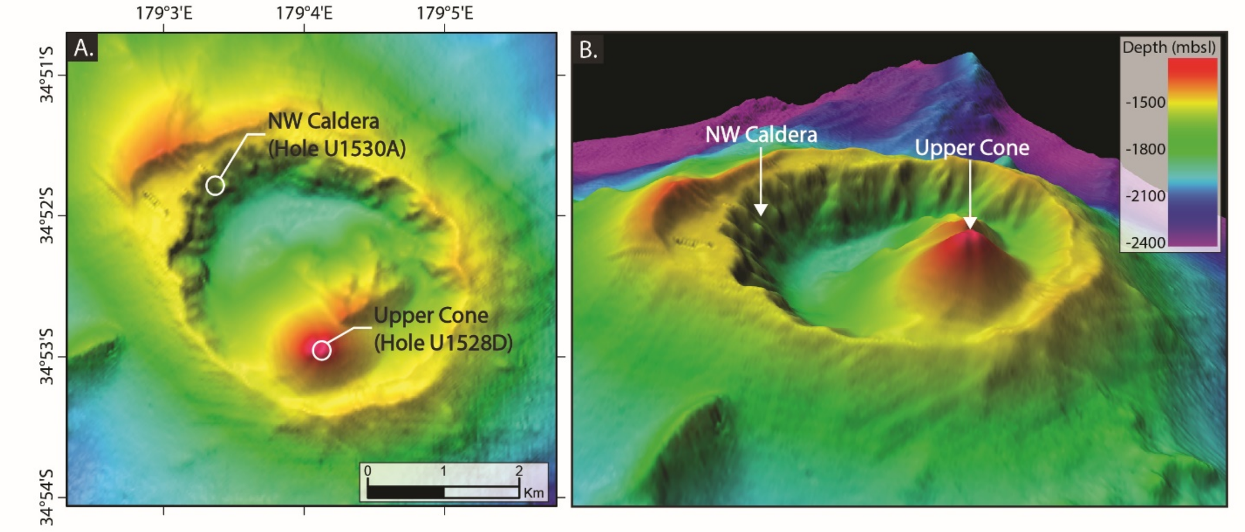
179°3'E
179°4'E
179°5'E
34°51'S
34°52'S
34°53'S
34°54'S
A.
NW Caldera
(Hole U1530A)
Upper Cone
(Hole U1528D)
0
1
2
Km
B.
NW Caldera
Upper Cone
Depth (mbsl)
-1500
-1800
-2100
-2400

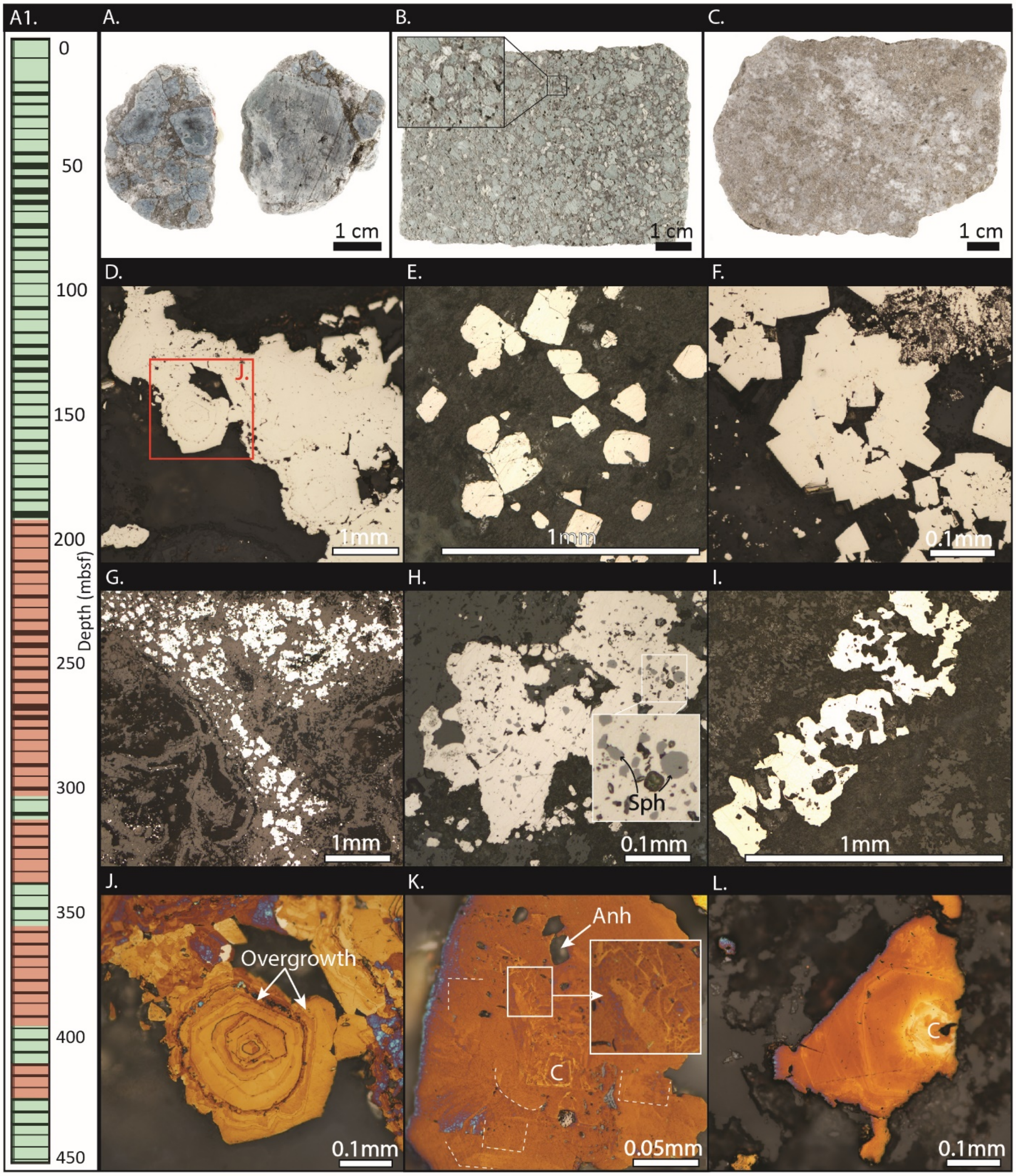
A1.
A.
B.
C.
0
50
100
150
200
250
300
350
400
450
Depth (mbsf)
1 cm
1 cm
1 cm
D.
E.
F.
J.
1mm
1mm
0.1mm
G.
H.
I.
Sph
1mm
0.1mm
1mm
J.
K.
L.
Overgrowth
Anh
C
C
0.1mm
0.05mm
0.1mm

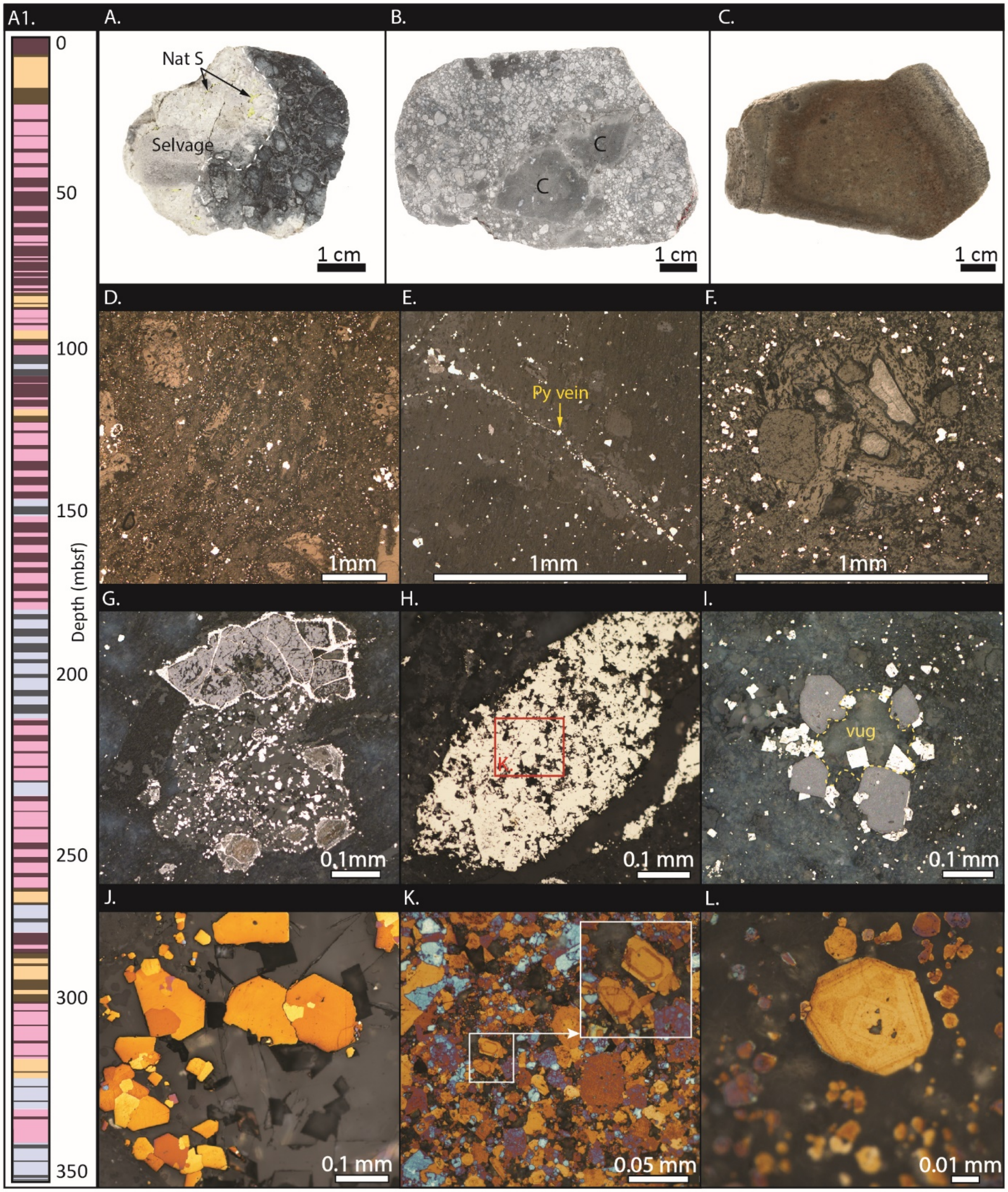
A1.
0
50
100
150
200
250
300
350
Depth (mbsf)
A.
Nat S
Selvage
1 cm
B.
C
C
1 cm
C.
1 cm
D.
1mm
E.
Py vein
1mm
F.
1mm
G.
0.1mm
H.
K
0.1 mm
I.
vug
0.1 mm
J.
0.1 mm
K.
0.05 mm
L.
0.01 mm

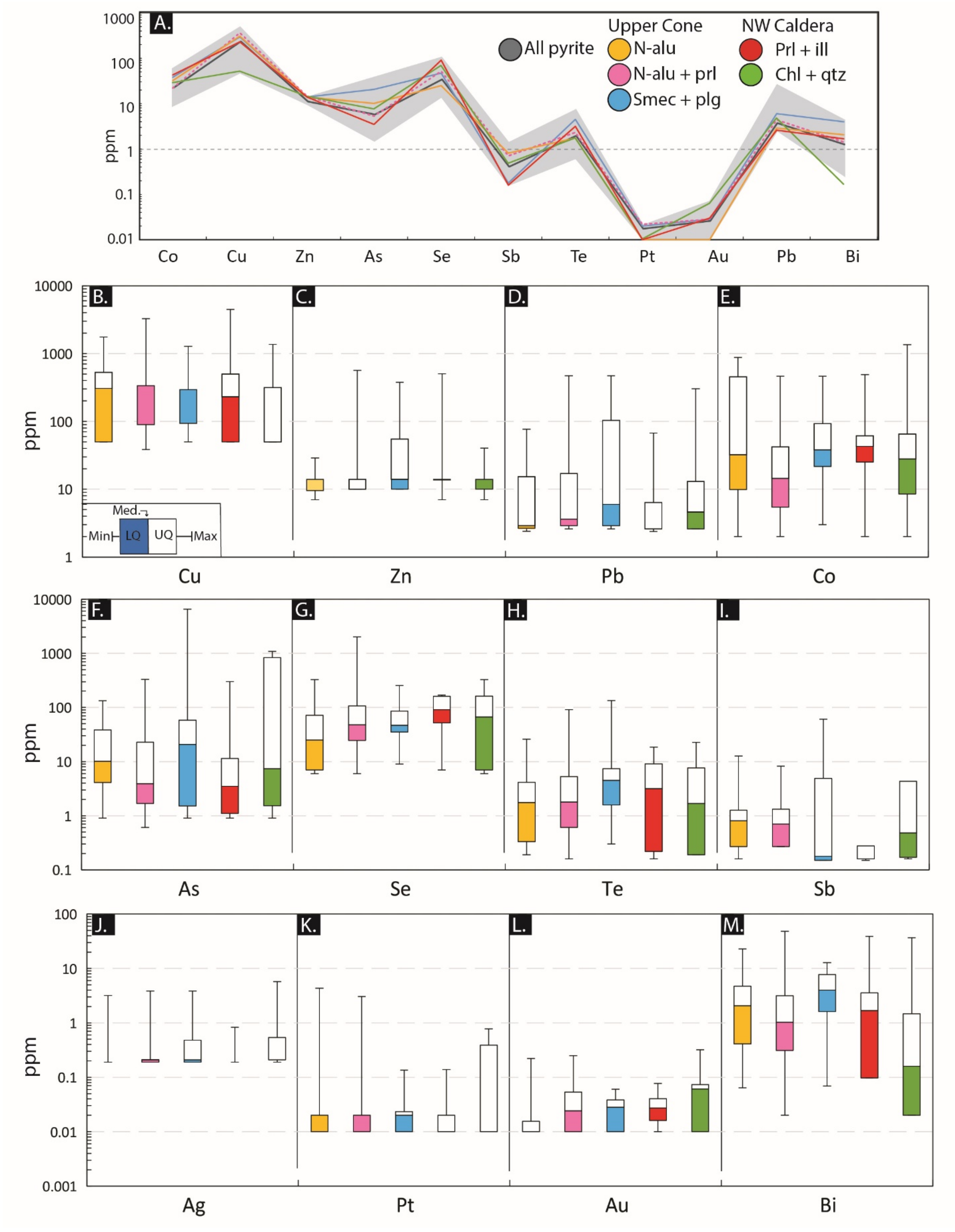
A.
1000
100
10
1
0.1
0.01
ppm
All pyrite
Upper Cone
N-alu
N-alu + prl
Smec + plg
NW Caldera
Prl + ill
Chl + qtz
Co
Cu
Zn
As
Se
Sb
Te
Pt
Au
Pb
Bi
B.
C.
D.
E.
10000
1000
100
10
1
ppm
Med.
Min
LQ
UQ
Max
Cu
Zn
Pb
Co
F.
G.
H.
I.
10000
1000
100
10
1
0.1
ppm
As
Se
Te
Sb
J.
K.
L.
M.
100
10
1
0.1
0.01
0.001
ppm
Ag
Pt
Au
Bi

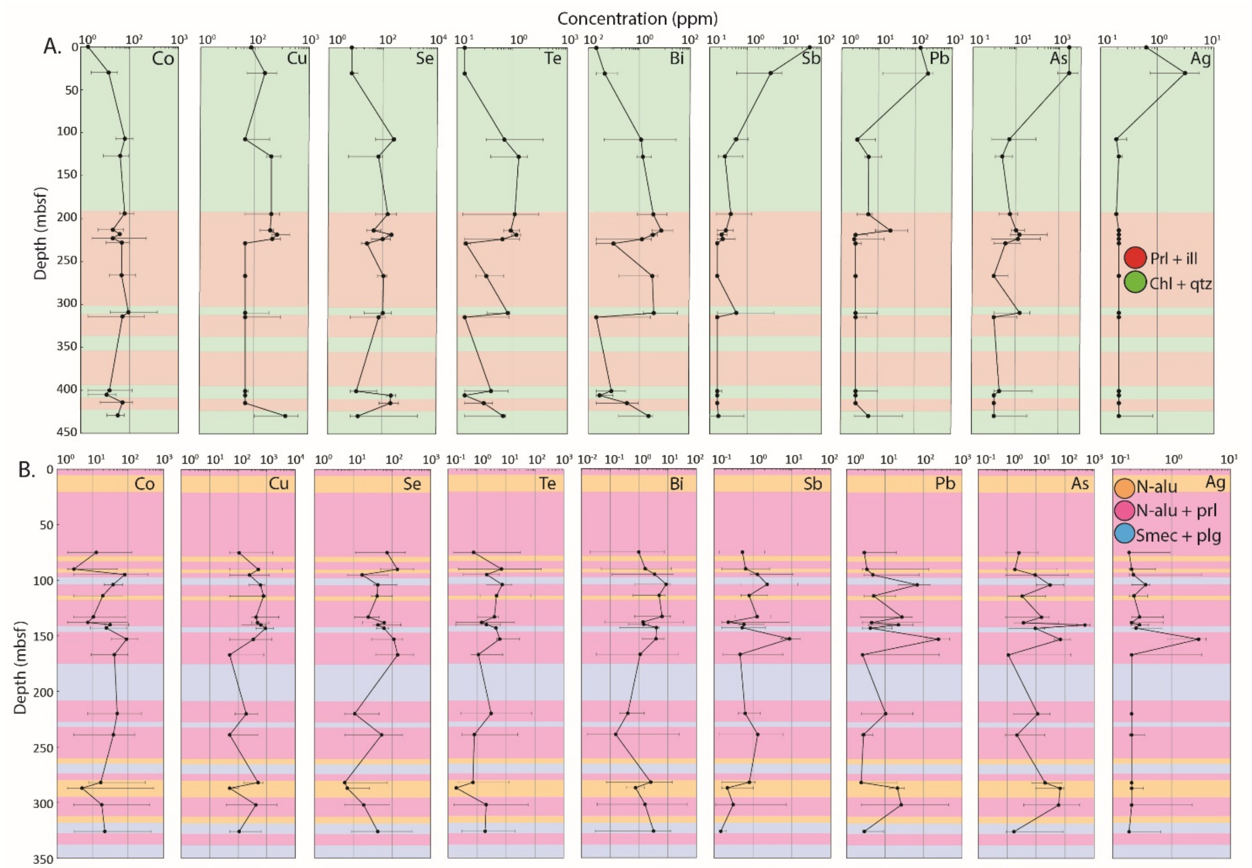
Concentration (ppm)
A.
B.
Depth (mbsf)
Co
Cu
Se
Te
Bi
Sb
Pb
As
Ag
Prl + ill
Chl + qtz
N-alu
N-alu + prl
Smec + plg
0
50
100
150
200
250
300
350
400
450

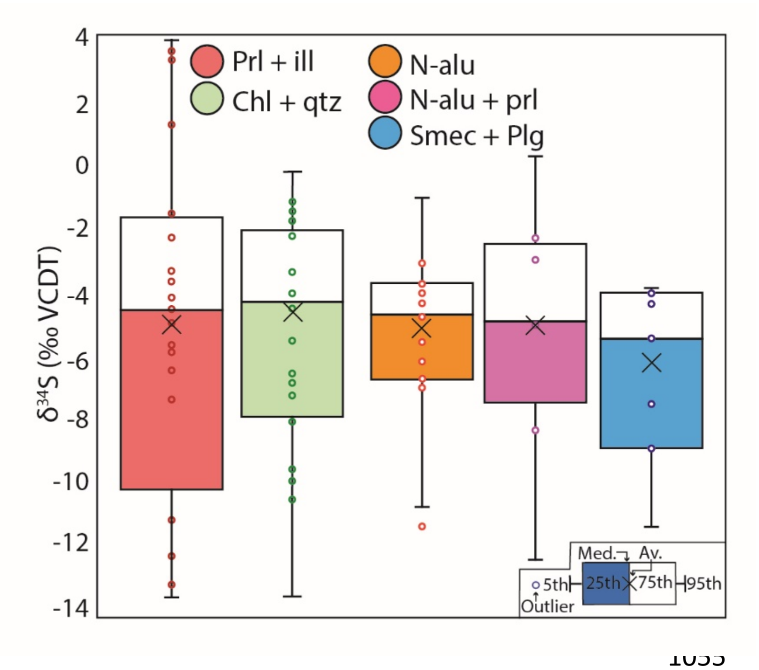
$\delta^{34}S$ (‰ VCDT)
4
2
0
-2
-4
-6
-8
-10
-12
-14
Prl + ill
Chl + qtz
N-alu
N-alu + prl
Smec + Plg
Med.
Av.
5th
25th
75th
95th
Outlier

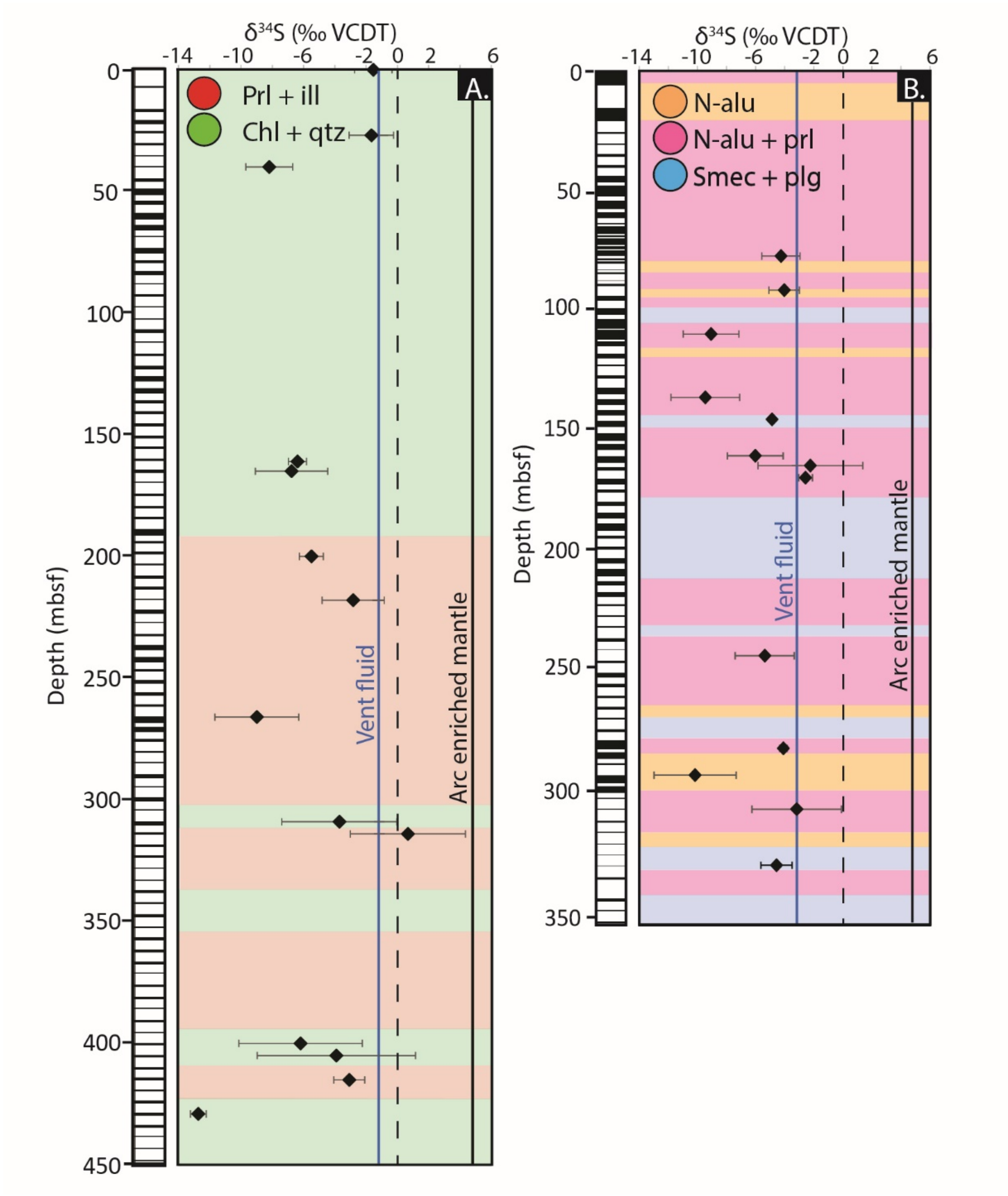
δ34S (‰ VCDT)
-14
-10
-6
-2
0
2
6
A.
Prl + ill
Chl + qtz
Depth (mbsf)
0
50
100
150
200
250
300
350
400
450
Vent fluid
Arc enriched mantle
δ34S (‰ VCDT)
-14
-10
-6
-2
0
2
6
B.
N-alu
N-alu + prl
Smec + plg
Depth (mbsf)
0
50
100
150
200
250
300
350
Vent fluid
Arc enriched mantle

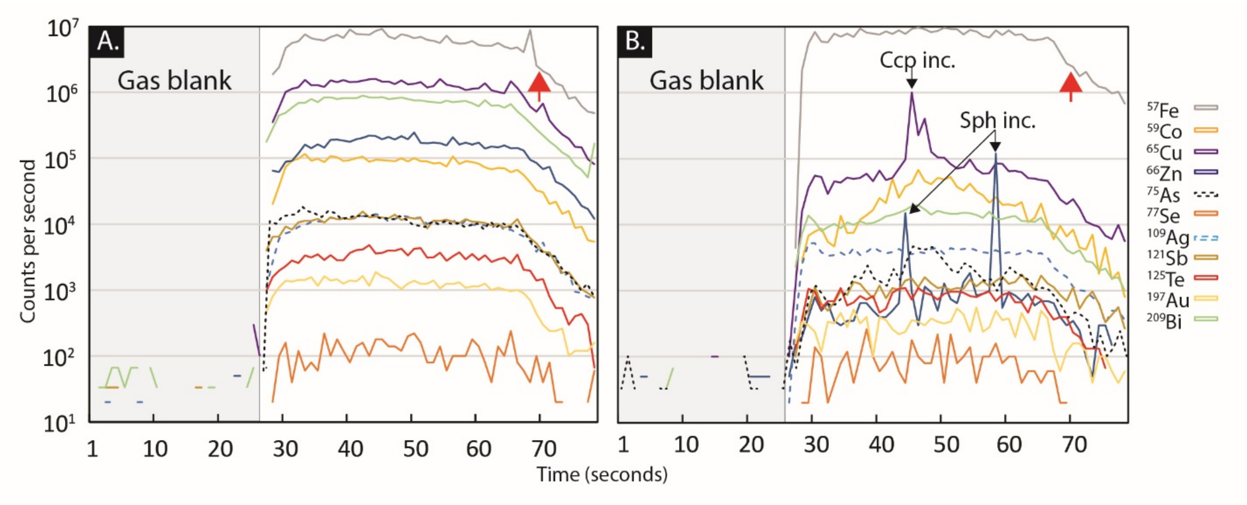
A.
B.
Gas blank
Gas blank
Ccp inc.
Sph inc.
Counts per second
Time (seconds)
10^7
10^6
10^5
10^4
10^3
10^2
10^1
1
10
20
30
40
50
60
70
57Fe
59Co
65Cu
66Zn
75As
77Se
109Ag
121Sb
125Te
197Au
209Bi

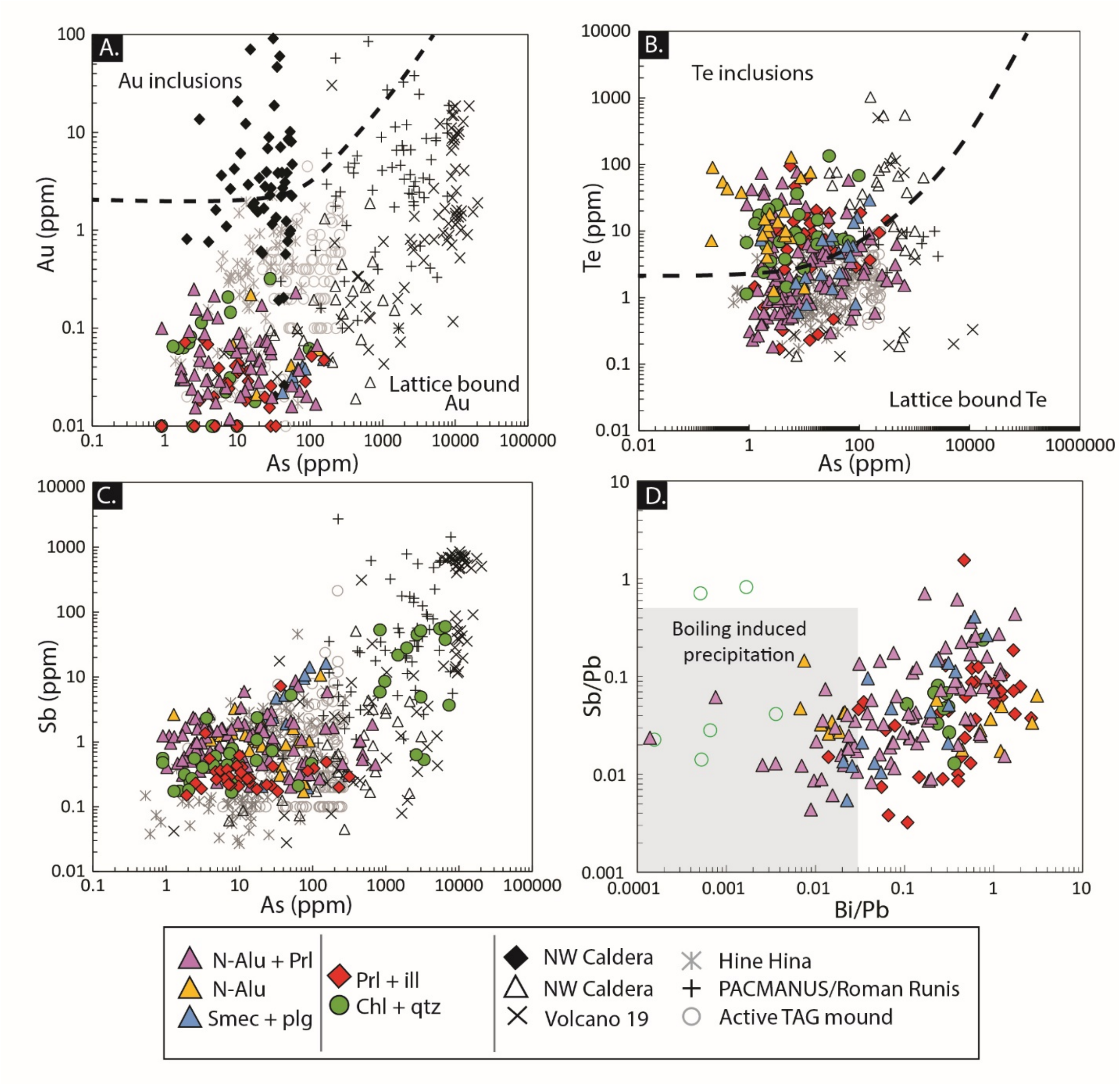
A.
Au inclusions
Lattice bound Au
Au (ppm)
As (ppm)
100
10
1
0.1
0.01
0.1
1
10
100
1000
10000
100000
B.
Te inclusions
Lattice bound Te
Te (ppm)
As (ppm)
10000
1000
100
10
1
0.1
0.01
0.01
1
100
10000
1000000
C.
Sb (ppm)
As (ppm)
10000
1000
100
10
1
0.1
0.01
0.1
1
10
100
1000
10000
100000
D.
Boiling induced precipitation
Sb/Pb
Bi/Pb
10
1
0.1
0.01
0.001
0.0001
0.001
0.01
0.1
1
10
N-Alu + Prl
N-Alu
Smec + plg
Prl + ill
Chl + qtz
NW Caldera
NW Caldera
Volcano 19
Hine Hina
PACMANUS/Roman Runis
Active TAG mound

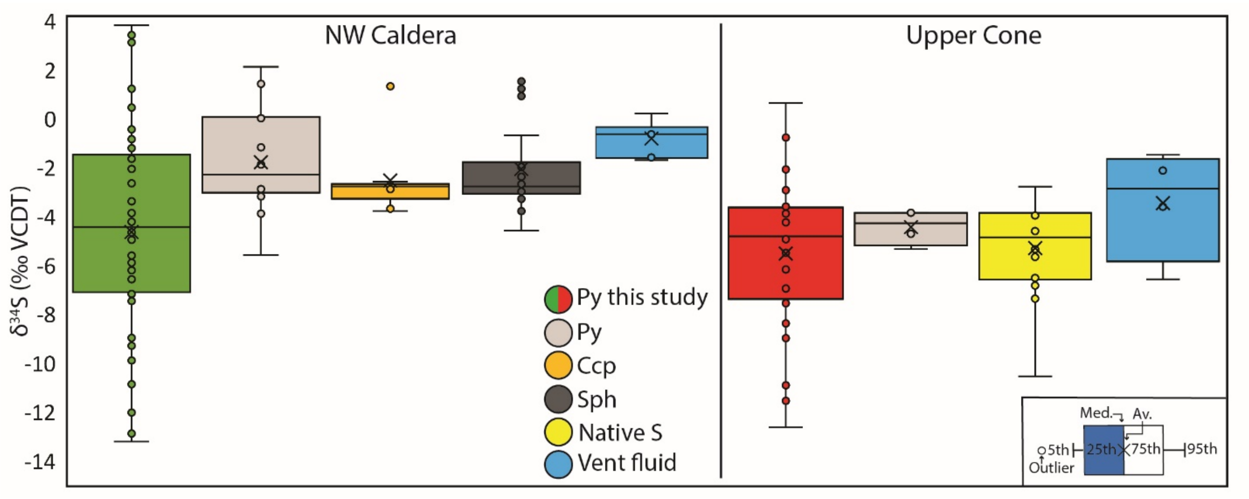
NW Caldera
Upper Cone
δ^{34}S (‰ VCDT)
4
2
0
-2
-4
-6
-8
-10
-12
-14
Py this study
Py
Ccp
Sph
Native S
Vent fluid
Med.
Av.
5th
25th
75th
95th
Outlier

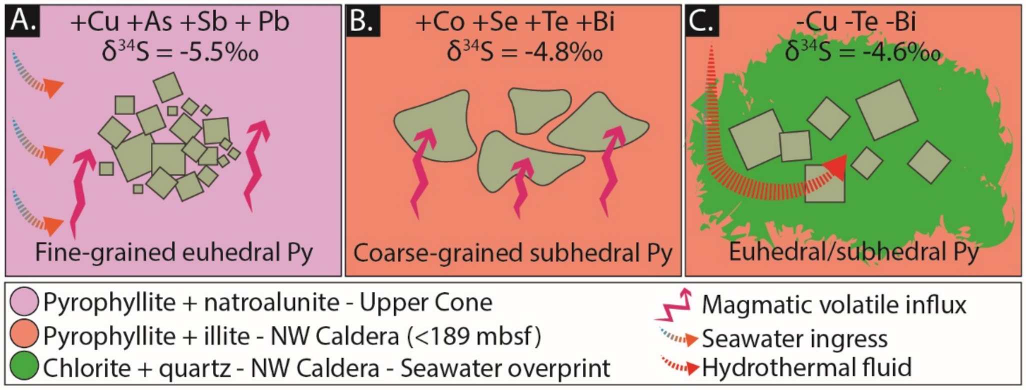
A.
+Cu +As +Sb + Pb
δ34S = -5.5‰
Fine-grained euhedral Py
B.
+Co +Se +Te +Bi
δ34S = -4.8‰
Coarse-grained subhedral Py
C.
-Cu -Te -Bi
δ34S = -4.6‰
Euhedral/subhedral Py
Pyrophyllite + natroalunite - Upper Cone
Pyrophyllite + illite - NW Caldera (<189 mbsf)
Chlorite + quartz - NW Caldera - Seawater overprint
Magmatic volatile influx
Seawater ingress
Hydrothermal fluid

		Co	Ni	Cu	Zn	As	Se	Pd	Ag	Cd	Sb	Te	Re	Pt	Au	Pb	Bi
		ppm	wt%	wt%	ppm	ppm	ppm	ppm	ppm	ppm	ppm	ppm	ppm	ppm	ppm	ppm	ppm
NW Caldera																	
Chl + qtz	Av.	81.7	0.02	0.02	13.0	886.4	104.8	0.06	0.58	0.24	7.54	9.02	0.02	0.02	0.07	42.9	2.26
n=53	Med.	27.8	0.01	0.01	14.0	7.37	66.8	0.06	0.21	0.25	0.47	1.69	0.02	0.01	0.06	4.61	0.16
	Max	1351.7	0.05	0.10	40.3	7323.5	328.9	0.07	5.56	0.25	59.8	134.2	0.16	0.40	0.32	303.2	36.8
	σ	233.5	0.02	0.02	5.35	1853.0	107.9	0.00	1.03	0.01	16.5	20.9	0.02	0.06	0.08	79.1	6.61
Prl + ill	Av.	66.3	0.02	0.04	24.4	18.1	152.2	0.06	0.22	0.31	0.34	7.49	0.03	0.02	0.03	7.54	2.93
n=76	Med.	42.9	0.01	0.02	14.0	3.49	91.0	0.06	0.21	0.25	0.16	3.17	0.02	0.01	0.03	2.60	1.68
	Max	487.3	0.09	0.45	503.6	319.5	2075.4	0.09	0.83	4.21	7.20	94.9	0.42	0.14	0.08	67.2	23.7
	σ	85.0	0.02	0.07	59.0	49.1	270.1	0.01	0.07	0.46	0.82	14.03	0.05	0.02	0.02	11.9	4.29
Upper Cone																	
Smec + plg	Av.	82.1	0.01	0.04	44.9	33.5	75.7	0.06	0.76	0.24	3.06	6.20	0.02	0.03	0.03	76.9	4.86
n=28	Med.	38.1	0.01	0.03	14.0	20.6	47.0	0.06	0.21	0.22	0.18	4.51	0.02	0.02	0.03	6.01	3.99
	Max	463.7	0.01	0.15	376.3	152.8	342.2	0.15	3.84	0.46	16.3	29.3	0.05	0.14	0.06	471.0	12.8
	σ	101.5	0.00	0.03	76.6	38.1	71.7	0.02	1.12	0.04	4.70	6.72	0.01	0.04	0.02	126.0	4.01
N-alu + prl	Av.	45.4	0.02	0.04	31.0	38.8	74.7	0.06	0.39	0.26	1.42	8.25	0.07	0.05	0.04	32.5	3.23
n=151	Med.	20.3	0.01	0.03	13.5	4.87	47.5	0.06	0.21	0.25	0.65	2.12	0.02	0.02	0.03	4.01	1.31
	Max	463.7	0.05	0.35	563.0	727.8	362.5	0.15	3.84	1.79	16.3	170.1	1.58	3.04	0.25	471.0	48.1
	σ	76.3	0.02	0.05	71.4	99.5	72.8	0.01	0.61	0.14	2.51	20.1	0.14	0.24	0.04	79.0	5.54
N-alu	Av.	86.4	0.01	0.04	12.7	25.7	51.2	0.06	0.35	0.24	1.13	2.57	0.02	0.14	0.03	10.4	3.79
n=37	Med.	32.0	0.01	0.03	14.0	10.1	24.9	0.06	0.21	0.25	0.81	1.75	0.02	0.02	0.01	2.90	2.06
	Max	522.6	0.05	0.18	28.9	129.0	363.3	0.06	3.18	0.25	10.7	13.0	0.13	4.36	0.22	76.5	22.7
	σ	121.2	0.02	0.04	4.97	31.4	69.9	0.01	0.51	0.01	1.76	2.99	0.02	0.71	0.05	14.1	5.03